STABLE HIGH CONDUCTIVITY BILAYERED ELECTROLYTES FOR LOW TEMPERATURE SOLID OXIDE FUEL CELLS

FETC AAD Document Control Bldg. 921
U.S. Department of Energy
Federal Energy Technology Center
P.O. Box 10940
Pittsburgh, PA 15236-0940

Contract # DE-AC26-99FT40712

Program Manager: Wayne Surdoval

Annual Report for Period 10/1/99 – 9/30/2000

Eric D. Wachsman
Department of Materials Science and Engineering
University of Florida
Gainesville, FL 32611-6400

CONTENTS

INTRODUCTION

Solid oxide fuel cells (SOFCs) are the future of energy production in America. They offer great promise as a clean and efficient process for directly converting chemical energy to electricity while providing significant environmental benefits (they produce negligible CO, HC, or NO_x and, as a result of their high efficiency, produce about one-third less CO_2 per kilowatt hour than internal combustion engines).

Unfortunately, the current SOFC technology, based on a stabilized zirconia electrolyte, must operate in the region of 1000°C to avoid unacceptably high ohmic losses. These high temperatures demand (a) specialized (expensive) materials for the fuel cell interconnects and insulation, (b) time to heat up to the operating temperature and (c) energy input to arrive at the operating temperature. Therefore, if fuel cells could be designed to give a reasonable power output at lower temperatures tremendous benefits may be accrued, not the least of which is reduced cost. The problem is, at lower temperatures the conductivity of the conventional stabilized zirconia electrolyte decreases to the point where it cannot supply electrical current efficiently to an external load.

The primary objectives of the proposed research is to develop a stable high conductivity (>0.05 S cm^{-1} at 550 °C) electrolyte for lower temperature SOFCs. This objective is specifically directed toward meeting the lowest (and most difficult) temperature criteria for the 21st Century Fuel Cell Program. Meeting this objective provides a potential for future transportation applications of SOFCs, where their ability to directly use hydrocarbon fuels could permit refueling within the existing transportation infrastructure.

In order to meet this objective we are developing a functionally gradient bilayer electrolyte comprised of bismuth oxide on the air side and ceria on the fuel side. Bismuth oxide and doped ceria are among the highest ionic conducting electrolytes and in fact bismuth oxide based electrolytes are the only known solid oxide electrolytes to have an ionic conductivity that meets the program conductivity goal.

We have previously demonstrated that this concept works, that a bismuth oxide/ceria bilayer electrolyte provides near theoretical open circuit potential (OCP) and is stable for 1400 h of fuel cell operation under both open circuit and maximum power conditions. More recently, we developed a computer model to determine the defect transport in this bilayer and have found that a bilayer comprised primarily of the more conductive component (bismuth oxide) is stable for 500°C operation.

In this first year of the project we are obtaining necessary thermochemical data to complete the computer model as well as initial SOFC results based on thick 1-2 mm single and bilayer ceria/bismuth oxide electrolytes. We will use the computer model to obtain the optimum relative layer thickness as a function of temperature and air/fuel conditions. SOFCs will be fabricated with 1-2 mm single and bilayer electrolytes based on the modeling results, tested for OCP, conductivity, and stability and compared against the predictions.

The computer modeling is a continuation of previous work under support from GRI and the student was available at the inception of the contract. However, the experimental effort was delayed until the beginning of the Spring Semester because the contract was started in October, 2 months after the start of our Fall Semester, and after all of the graduate students were committed to other projects. The results from both of these efforts are described in the following two sections: 1. Experimental; and 2. Computer Modeling.

1. EXPERIMENTAL

1.1 Apparatus Set Up

The SOFC sample holder and furnace (Figure 1.1), gas manifold/flow system, and electrochemical instrumentation were fabricated/assembled. The SOFC is sealed between glass O-rings and the steel mating flanges. The gas flow system consists of five Edwards 825 mass flow controllers, a 1605 interface/controller, and a stainless steel manifold for O_2, N_2, H_2, CH_4, and He (through an H_2O bubbler). Temperature control is by an Eurotherm 2408 temperature controller. The electrochemical instrumentation includes a Solartron 1287 Electrochemical Interface and a Keithly 2000 scanning multimeter, computer interfaced through a GPIB bus.

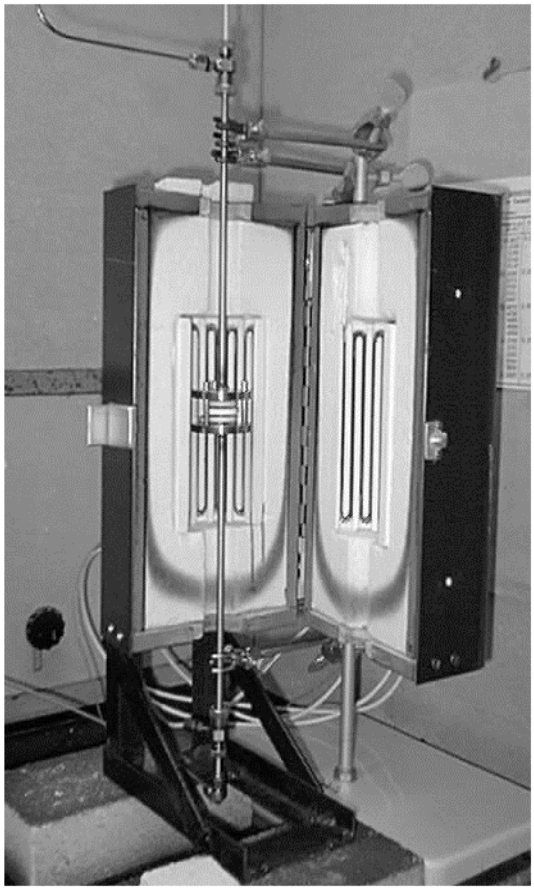

Figure 1.1 SOFC, including: machined steel housing with glass seals; modified furnace; and gas flow system.

1.2 Electrolyte Fabrication

Much of the progress achieved this semester by the students involved familiarizing themselves with laboratory equipment and processing procedures, and ordering required chemicals and processing equipment. Electrolyte fabrication consisted of synthesis of ceria and bismuth oxide disks, and determination of appropriate processing conditions as described below.

1.2.1 Ceria

We produced and evaluated several samaria-doped ceria (SDC) samples and started looking into the effects of various processing parameters (such as calcining temperature and uniaxial pressing pressure) and the effect of isostatic pressing on density and cracking of SDC samples.

Appropriate amounts of samaria powder and ceria powder to yield $Sm_xCe_{1-x}O_{2-2x}$, with x=0.2 were ball milled with zirconia grinding media in ethyl alcohol for 24 hours. The solvent was then evaporated on a hot plate. The dried powder was placed in an alumina crucible and calcined for 12 hours at 1100°C or 1200°C, or for 10 hours at 1300°C. XRD analysis was performed to determine phase composition and lattice parameters for density measurement. All of the powders had the expected fluorite pattern with no indication of a second phase.

The calcined powders were mechanically ground with mortar and pestle and shaken in 325 (40 micron) mesh sieves for about 45 minutes. This process was repeated until enough sieved powder was available to press a green body. A few grams of sieved powders were placed into a 1 1/8" cylindrical die and pressed uniaxially at pressures ranging from 1150 psi to 1400 psi. Isostatic pressing at 200 MPa was also performed on several of the samples.

These samples were then sintered at temperatures of 1450°C to 1650°C for 15 hours. The resulting dense bodies were polished to a thickness of approximately 2mm using sandpaper, ranging from 240 grit to 800 grit. Archimedes' principle was used to measure the density of the polished samples, and the measured densities were compared to the theoretical densities to give the percent theoretical densities for each sample.

Table 1.1 shows the processing conditions along with density results and observed sample flaws for each sample prepared this semester. It should be noted that the highest density was achieved at the highest sintering temperature (1650°C). However, due to the limitations of the furnace, this sintering temperature could not be reproduced. Also, cracks appeared on samples that were pressed at higher uniaxial pressures. Thus, one of the near-term goals for the students is to find the optimum processing conditions that will yield high densities at relatively low sintering temperatures, around 1450°C.

Table 1.1 Sample Processing Parameters and Density Results

Calcining Temperature (°C)	Sintering Temperature (°C)	Uniaxial Pressure (psi)	Isostatic Pressing (200 MPa)	Sample Flaws	% Theoretical Density
1100	1650	1400	No	Light ring crack, white spots	97.4
1100	1450	1400	No	Large cracks, dark spots	90.4
1100	1465	1350	Yes	Light cracking	88.7
1100	1465	1250	Yes	Edge chipping	88.7
1100	1465	1200	Yes	Good--no apparent flaws	88.7
1100	1465	1150	Yes	Good--no apparent flaws	88.0
1200	1450	1400	No	Ring crack	69.0

Platinum paste was painted on either side of the 97.4%-theoretical-density sample to serve as electrodes. After the initial painting, the samples were placed in an oven and dried at 130°C for 30 minutes. Once dried the sample was placed in a furnace and sintered at 1000°C for approximately 20 minutes to promote adhesion. A second coat of platinum paste was applied to ensure a continuous conductive path on both sides of the sample. This was then checked using a multimeter to measure the resistance across either electrode. The resistance obtained was well below 1Ω (hence the platinum coating was sufficient). Next thin (0.1mm diameter) gold wires were attached to both electrodes as leads and sintered at 1000°C for 10 minutes.

Conductivity measurements were performed on this sample using a Solartron Frequency Response Analyzer. The results are currently being analyzed. These results will be compared with those of the 69.0%-theoretical-density sample to help distinguish between bulk and grain boundary contributions to the total conductivities.

1.2.2 Bismuth Oxide

Several disk shaped pellets of $(Er_2O_3)_{0.2}$ $(Bi_2O_3)_{0.8}$ were prepared using the same procedure described above for ceria except that calcining of the powders was done at 800°C for 16 hours, and sintering was done at 890°C for 16 hours. Our investigation of the structural stability and effect of structure on the conductivity of bismuth oxides was continued. The results of that investigation are presented in the two papers; "Neutron Diffraction Study of Aging Phenomenon and Oxygen Ion Transport in Phase-Stabilized Cubic Bismuth Oxides," and "Effect of Oxygen Sublattice Ordering on Interstitial Transport Mechanism and Conductivity Activation Energies in Phase-Stabilized Cubic Bismuth Oxides;" for submission to Solid State Ionics and attached in the Appendix.

2. COMPUTER MODELING

2.1 Overview

In the last six months several significant hurdles have been cleared. These achievements may be grouped into three areas. Firstly, we have been able to refine the equations for defect distribution and extend it to another important MIEC family, namely $La_{1-x}Sr_xFe_{1-y}Co_yO_{3-\delta}$ (LSCF). This will allow us to look at the potential drop through the cathode layer in solid oxide fuel cells. Secondly, we have identified methods by which the electronic mobility u_e and the most crucial of the defect equilibrium constants K_R , can be determined through a combination of

experiment and theory. Finally, we have improved the formulation of the equations for defect flux.

In the remainder of the report we will briefly review the changes made to the model and summarize its current state of development.

2.2 Functional Dependences of Defect Concentrations on Pressure and Distance in SDC

2.2.1 The Influence of Small Polaron Formation

In modeling the defect equilibria of samaria doped ceria (SDC) we initially treated the Ce'_{Ce} defect species as totally distinct from the electronic defects, e'. This resulted in the model "counting" the electronic species twice. On reviewing our approach we realized that since the Ce'_{Ce} defect consists of an electron "sitting" on a $Ce^{\times}_{Ce}$ atom. Therefore, when the concentration of electrons, $n \leq [Ce^{\times}_{Ce}]$, the concentration of cerium cations, e' and Ce'_{Ce} are identical. e' and Ce'_{Ce} can only be treated separately when $n > [Ce^{\times}_{Ce}]$ — i.e., when the electron concentration exceeds the $Ce^{\times}_{Ce}$ cations the excess electrons must be treated as itinerant electrons.

The mechanism describing the trapping of electrons on $Ce^{\times}_{Ce}$ is called Small polaron formation and may be described by the following psuedo-thermodynamic reaction:

$$Ce^{\times}_{Ce} + e' \leftrightarrow Ce'_{Ce} \qquad \Rightarrow \qquad K_D(T) = \frac{[Ce'_{Ce}]}{[Ce^{\times}_{Ce}]n} \qquad (2.1)$$

where K_D is the equilibrium constant for the reaction. Since these cations are distributed between two valence states there is the requirement of conservation of the number of cations in the form of a mass balance equation given by:

$$[Ce'_{Ce}] + [Ce^{\times}_{Ce}] = Ce_{tot} \qquad (2.2)$$

Additionally, Eqs. (2.1) and (2.2) may be combined to yield:

$$[Ce'_{Ce}] = \frac{nK_D Ce_{tot}}{1 + nK_D} \tag{2.3}$$

Typically, the constraints imposed by small polaron formation are ignored when examining the defect equilibria, that is n is assumed to be equal to $[Ce'_{Ce}]$. However, since the population of small polarons cannot exceed that of the cations present in the lattice, ignoring said constraints may lead to an over estimation of the number of electrons which exist as small polarons. Hence, if there are more electrons than the number of cations, as mentioned earlier, they must be of the non-associated (i.e., itinerant) variety. That is

$$n = n_f + [Ce'_{Ce}] \tag{2.4}$$

where n_f refers to the electrons that are not associated with a cation. In the development of the model in the next section, only n will be considered for any mathematical treatment and $[Ce'_{Ce}]$ will be separated from n in the DEDs through Eq. (2.3).

Since for $n \leq [Ce^{\times}_{Ce}]$ all the electrons are trapped on a cation site in the form of $[Ce'_{Ce}]$ and $n_f = 0$, we may write:

$$\lim_{n_f \to 0} [Ce'_{Ce}] = n \tag{2.5}$$

which implies, from Eq. (2.1), that

$$\lim_{n \to 0} K_D = \lim_{n \to 0} \frac{[Ce'_{Ce}]}{[Ce^{\times}_{Ce}]n} = \lim_{n \to 0} \frac{[Ce'_{Ce}]}{(Ce_{tot} - [Ce'_{Ce}])n} = \lim_{n \to 0} \frac{n}{(Ce_{tot} - n)n} = \frac{1}{Ce_{tot}} \tag{2.6}$$

At first glance, this result seems to imply that the equilibrium constant K_D, is determined by the total concentration of cerium cations. However, this result is an artifact of expressing K_D in terms of concentrations instead of activities or mole fractions which would have made K_D dimensionless.

Rewriting K_D , Eq. (2.1), in terms of mole fractions, we have:

$$K_D = \frac{X_{Ce'_{Ce}}}{X_{Ce^{\times}_{Ce}}\breve{n}} \tag{2.7}$$

where $\breve{n} = n/N_c$. $\breve{n}$ is dimensionless and N_c is the density of states in the conduction band. Also, from Eq. (2.2):

$$X_{Ce'_{Ce}} + X_{Ce^{\times}_{Ce}} = 1 \tag{2.8}$$

Therefore, for $n \leq [Ce^{\times}_{Ce}]$, $n_f = 0$ — as in Eq. (2.5):

$$\lim_{n_f \to 0} X_{Ce'_{Ce}} = \breve{n} \tag{2.9}$$

and

$$\lim_{n\to 0} K_D = \lim_{n\to 0} \frac{X_{Ce'_{Ce}}}{X_{Ce^{\times}_{Ce}}\breve{n}} = \lim_{n\to 0} \frac{X_{Ce'_{Ce}}}{\left(1 - X_{Ce'_{Ce}}\right)\breve{n}} = \lim_{n\to 0} \frac{\breve{n}}{(1-\breve{n})\breve{n}} = 1 \tag{2.10}$$

Now, K_D is related to the activation energy of small polaron formation ΔG_D, by

$$K_D = \exp\left(-\frac{\Delta G_D}{RT}\right) \tag{2.11}$$

Therefore if $K_D = 1$, then $\Delta G_D = 0$. This result suggests that the "reaction" ($Ce^{\times}_{Ce} + e' \leftrightarrow Ce'_{Ce}$) to form small polarons is not characterized by an activation energy. This is reasonable since,

according to Madelung [1], the binding energy, E, of a small polaron in its potential well is given by:

$$E = -\frac{e^2}{16\pi\varepsilon_0 r_p}\left(\frac{1}{\varepsilon(\infty)} - \frac{1}{\varepsilon(0)}\right) = -\frac{m^* e^4}{128\pi^2\varepsilon_0^2\hbar^2}\left(\frac{1}{\varepsilon(\infty)} - \frac{1}{\varepsilon(0)}\right)^2 \qquad (2.12)$$

given

$$\frac{1}{r_p} = \frac{m^* e^2}{8\pi\varepsilon_0\hbar^2}\left(\frac{1}{\varepsilon(\infty)} - \frac{1}{\varepsilon(0)}\right) \qquad (2.13)$$

In the above equations: e is the charge on an electron; r_p is the radius of the small polaron, ε_0 is the permittivity of free space; $\varepsilon(\infty)$ is the relative permittivity outside the potential well and $\varepsilon(0)$ is the relative permittivity inside the potential well; m^* is the effective mass of the electron (small polaron); and $\hbar$ is Planck's constant.

None of the terms in the equation for the binding energy of a small polaron is characterized by an activation energy so the estimation of $\Delta G_D = 0$ seems appropriate.

2.2.2 Defect Concentration as a Function of Pressure

As before, we next develop a model for the functional dependences of defect concentrations on pressure. Again the model relaxes the usual assumption of constant vacancy concentration in the mixed conducting region but retains the assumption of a negligible concentration of holes and oxygen interstitials because it is justified by a numerical solution of the defect formation equations for ceria. Finally, in presenting the model the following symbol substitutions: $[V_O^{\bullet\bullet}] \equiv V$, $[Sm'_{Ce}] \equiv A$ and $P_{O_2} \equiv P$ are used.

The charge neutrality equation, in the *region of interest*, i.e., 2 atm. > P > 10^{-25} atm.:

$$n + A = 2V \qquad (2.14)$$

and the external equilibria

$$O_O^{\times} \leftrightarrow V_O^{\bullet\bullet} + 2e' + \frac{1}{2}O_2 \uparrow \qquad \Rightarrow \qquad K_R(T) = Vn^2 P_{O_2}^{\frac{1}{2}} \tag{2.15}$$

give intra-relationships between the significant defects, n and V, and the inter-relationships between those defect and the external partial pressure P. To understand how each variable responds to a small change in one of the other variables, we will examine the differential form of Eqs. (2.14) and (2.15). Differentiating, Eqs. (2.14) and (2.15) yields:

$$\partial n = 2\partial V \tag{2.16}$$

and

$$\frac{\partial K_R(T)}{\partial V} = 0 = n^2 P^{\frac{1}{2}} \frac{\partial V}{\partial V} + 2VnP^{\frac{1}{2}} \frac{\partial n}{\partial V} + \frac{Vn^2 P^{-\frac{1}{2}}}{2} \frac{\partial P}{\partial V} \tag{2.17}$$

$\partial K_R/\partial V = 0$ since K_R is a function of temperature only.

Substituting Eqs. (2.15) and (2.16) into Eq. (2.17) yields:

$$\frac{dP}{dV} + \frac{2}{V} P = -8V^{\frac{1}{2}} K_R^{-\frac{1}{2}} P^{\frac{5}{4}} \tag{2.18}$$

With the boundary condition of $\lim_{P \to \infty} V = \frac{1}{2}A$ at high P_{O_2}, for the region of interest, the solution of Eq. (2.18) is:

$$V(P) = \left[\frac{1}{2} K_R^{\frac{1}{2}} P^{-\frac{1}{4}} + \left(\frac{1}{2} A \right)^{\frac{3}{2}} \right]^{\frac{2}{3}} \tag{2.19}$$

The relationship, $n(P)$, may now be obtained by substituting Eq. (2.19) into Eq. (2.15) to get:

$$n(P) = K_R^{\frac{1}{2}} P^{-\frac{1}{4}} \left[\frac{1}{2} K_R^{\frac{1}{2}} P^{-\frac{1}{4}} + \left(\frac{1}{2} A \right)^{\frac{3}{2}} \right]^{-\frac{1}{3}} \qquad (2.20)$$

Eqs. (2.19) and (2.20) are plotted in Fig. 1 along with the numerically solved defect equations [2] for the relevant defect species and Porat and Tuller's [3] equation, the latter for additional verification of our results. The observed close fit demonstrates the validity and accuracy of the model in describing the defect equilibria of the aforementioned defect species in the "region of interest", i.e., from ambient atmospheric to reducing conditions (< 10^{-15} atm.).

Further analysis of Eqs. (2.19) and (2.20) shows that in highly reducing conditions (P < ~10^{-18} atm.), $\left(\frac{1}{2} A \right)^{\frac{3}{2}} << \frac{1}{2} K_R^{\frac{1}{2}} P^{-\frac{1}{4}}$ and therefore Eq. (2.19) and (2.20) reduce to:

$$V(P) \approx \left[\frac{1}{4} K_R \right]^{\frac{1}{3}} P^{-\frac{1}{6}} \qquad \text{and} \qquad n(P) \approx 2 \left[\frac{1}{4} K_R \right]^{\frac{1}{3}} P^{-\frac{1}{6}}$$

(2.21)

That is, $V(P) \propto P^{-\frac{1}{6}}$, $n(P) \propto P^{-\frac{1}{6}}$ and $n = 2V$.

Additionally, in the electrolytic region (P > 10^{-15} atm.), where V is constant and the proportion of vacancies due to doping with A is greater than that due to the reduction of ceria, the term $\left(\frac{1}{2} A \right)^{\frac{3}{2}} >> \frac{1}{2} K_R^{\frac{1}{2}} P^{-\frac{1}{4}}$. Hence, in this region Eqs. (2.19) and (2.20) reduce to

$$V(P) \approx \frac{1}{2} A \qquad \text{and} \qquad n(P) \approx K_R^{\frac{1}{2}} \left(\frac{1}{2} A \right)^{-\frac{1}{2}} P^{-\frac{1}{4}} \qquad (2.22)$$

That is, $V(P)$ is a constant and $n(P) \propto P^{-\frac{1}{4}}$.

The proportionality relationships in Eqs. (2.21) and (2.22) have been verified experimentally [4 - 7] and can be deduced [8] for SDC using the Brouwer [9] approach.

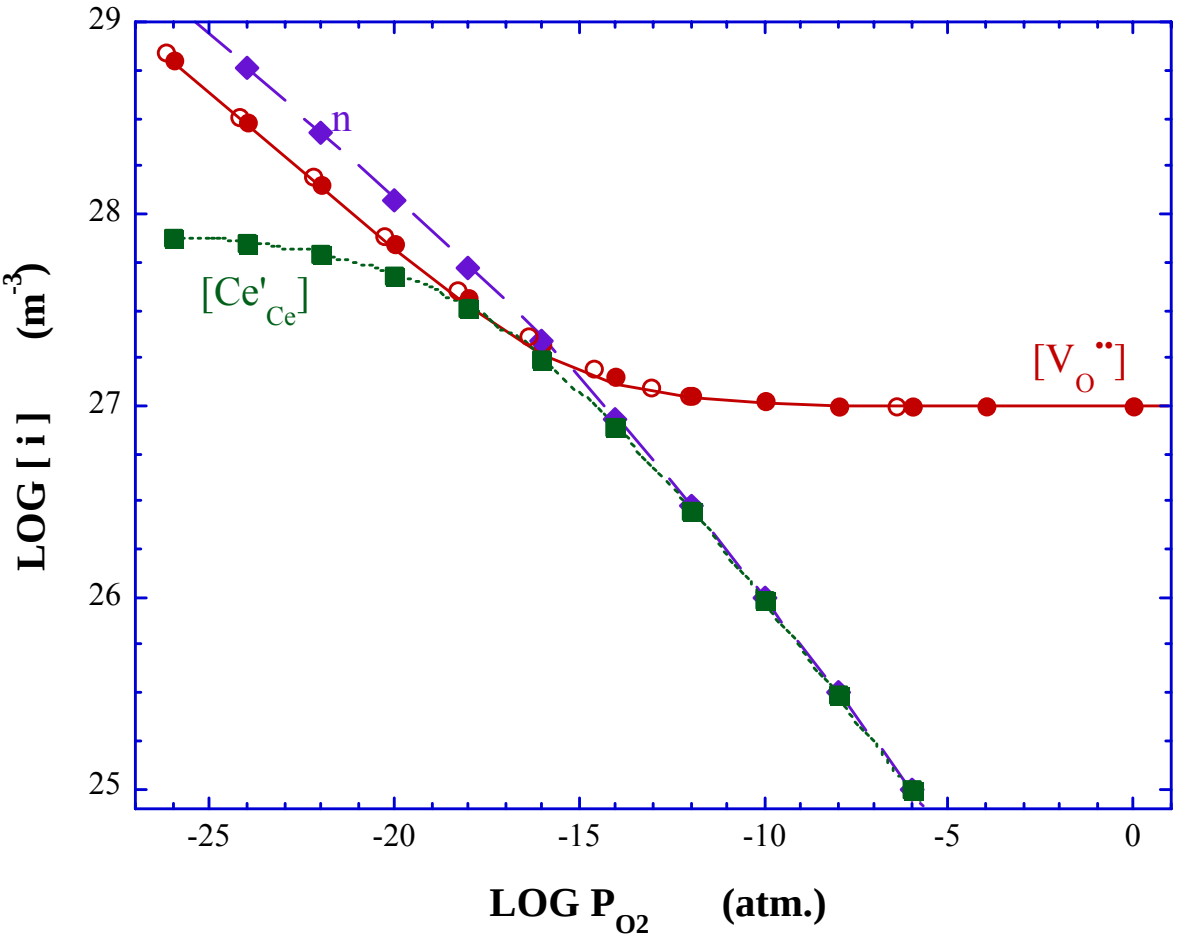

Figure 2.1 Comparison of SDC DED obtained: numerically [2] (solid symbols), model (lines), and Porat and Tuller [3] (open symbols).

2.2.3 Defect Concentration as a Function of Distance

As developed in an earlier paper [2], the equations derived for the defect concentrations as a function of oxygen partial pressure may be formulated as functions of distance for an MIEC in a oxygen potential gradient through the equation below

$$P(x) = P_0\left(\frac{P_L}{P_0}\right)^{\frac{x}{L}} \tag{2.23}$$

Eq. (2.23) describes the *effective* spatial P_{O_2} profile in the MIEC under steady state conditions and is consistent with the flux of oxygen, j_{O_2}, through the MIEC being constant at

steady state. Hence, since the concentration of defects in the MIEC depends on the prevailing P_{O_2}, the functional dependence of defect concentration on x may be obtained by substituting Eq. (2.23) into Eqs. (2.19) and (2.20) yielding:

$$V(x)=\left[\frac{1}{2}K_R^{\frac{1}{2}}P_0^{-\frac{1}{4}}\left(\frac{P_L}{P_0}\right)^{-\frac{x}{4L}}+\left(\frac{1}{2}A\right)^{\frac{3}{2}}\right]^{\frac{2}{3}} \tag{2.24}$$

and

$$n(x)=K_R^{\frac{1}{2}}P_0^{-\frac{1}{4}}\left(\frac{P_L}{P_0}\right)^{-\frac{x}{4L}}\left[\frac{1}{2}K_R^{\frac{1}{2}}P_0^{-\frac{1}{4}}\left(\frac{P_L}{P_0}\right)^{-\frac{x}{4L}}+\left(\frac{1}{2}A\right)^{\frac{3}{2}}\right]^{-\frac{1}{3}} \tag{2.25}$$

Eqs. (2.24) and (2.25) are plotted in Fig. 2.2 showing the spatial distribution of vacancies and electrons inside SDC. In the plot one may observe that for $x/L \geq \sim 0.5$, $n(x)$ becomes much smaller then $V(x)$ as the MIEC approaches the character of an electrolyte. Fig. 2.2 also compares the spatial distribution of n with and without the assumption of constant V. The plot shows that the curve depicting $n(x)$ for an assumed constant V, gives higher values of $n(x)$ compared to the curve for which that assumption is not made. This is a consequence of Eq. (2.15) from which one may deduce that assuming a constant V forces n to modulate more extremely with P. Conversely, if V is allowed to increase while n also increases (or decrease while n also decreases) then the degree of modulation of n with P is reduced. In other words, if V is not constrained to be constant then, for any change in the P, the corresponding change in n is smaller.

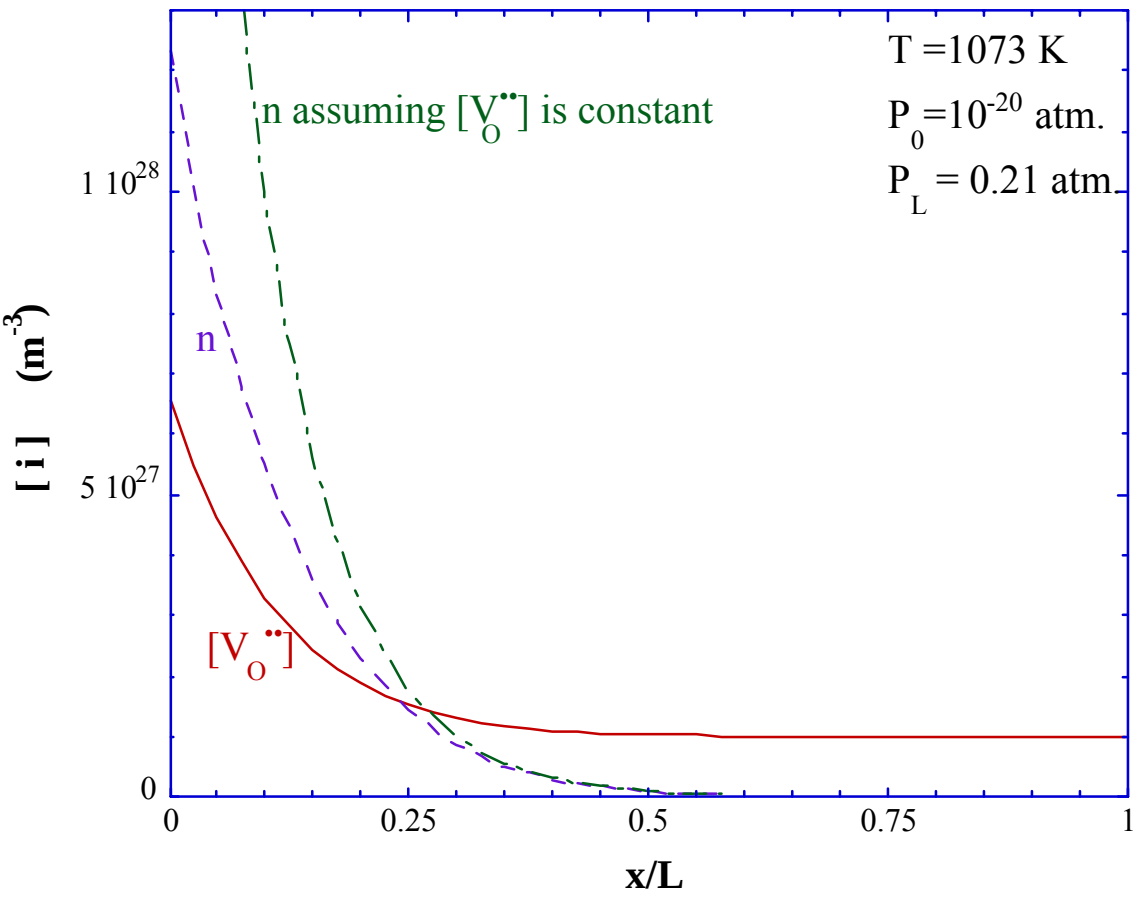

Figure 2.2 *V*(*x*) and *n*(*x*) vs. *x*/*L*

2.3 Extending the Model: Functional Dependence of Defect Concentrations on P_{O_2} in LSCF

The model had previously been extended to include bismuth oxide [10] and the following relationships were derived:

$$V(P) = \frac{1}{16}\left[\left(8[B_{tot}] + K_{ox}P^{\frac{1}{2}}\right)^{\frac{1}{2}} - K_{ox}^{\frac{1}{2}}P^{\frac{1}{4}}\right]^2 \qquad (3.1)$$

and

$$p(P) = \frac{1}{4}\left(-K_{0x}P^{\frac{1}{2}} + \sqrt{8[Bi_{Fl}']K_{0x}P^{\frac{1}{2}} + K_{0x}^2 P} \right) \tag{3.2}$$

To complete our analysis of typical oxide ion conducting oxides we will now obtain the functional dependences of defect concentrations on pressure for LSCF which is representative of *typical* perovskite MIECs.

The defect equilibrium equations governing defect formation in LSCF are given below:

Oxide-Oxygen Gas Equilibrium

At *low* P_{O_2}:

$$O_O^{\times} \leftrightarrow V_O^{\bullet\bullet} + 2e' + \frac{1}{2}O_2 \qquad \Rightarrow \qquad K_{R2}(T) = [V_O^{\bullet\bullet}]n^2 P_{O_2}^{\frac{1}{2}} \tag{3.3}$$

At *high* P_{O_2}:

$$V_O^{\bullet\bullet} + \frac{1}{2}O_2 \leftrightarrow O_O^{\times} + 2h^{\bullet} \qquad \Rightarrow \qquad K_{OX2}(T) = \frac{p^2}{[V_O^{\bullet\bullet}]P_{O_2}^{\frac{1}{2}}} \tag{3.4}$$

and if we multiply Eq. (3.3) by Eq. (3.4) we get

$$K_{OX2}K_{R2} = K_i^2 \tag{3.5}$$

B-site Schottky Disorder (*B* ≡ *Fe*, *Co*)

$$2B_B^{\times} + 3O_O^{\times} \leftrightarrow 2V_B'''' + 3V_O^{\bullet\bullet} + B_2O_3(\mathrm{s}) \qquad \Rightarrow \qquad K_S(T) = [V_B'''']^2[V_O^{\bullet\bullet}]^3 \tag{3.6}$$

Intrinsic, Electron-Hole Pair Formation

$$null \rightarrow e' + h^{\bullet} \qquad \Rightarrow \qquad K_i(T) = np \tag{3.7}$$

Fixed-Valence-Acceptor Doping on the A-Site

$$2SrO \xrightarrow{LaFeO_3} 2Sr'_{La} + V_O^{\bullet\bullet} + 2O_O^{\times} \tag{3.8}$$

or

$$SrO \xrightarrow{LaFeO_3} Sr'_{La} + h^{\bullet} + O_O^{\times} \tag{3.9}$$

Isovalent Doping on the *B*-Site

$$LaCoO_3 \xrightarrow{LaFeO_3} La_{La}^{\times} + Co_{Fe}^{\times} + 3O_O^{\times} \tag{3.10}$$

B-site Small Polaron Formation ($B \equiv$ *Fe, Co*)

For $p <<< n$:

$$B_B^{\times} + e' \leftrightarrow B'_B \qquad \Rightarrow \qquad K_{spe} = \frac{[B'_B]}{[B_B^{\times}]n} \tag{3.11}$$

For $n <<< p$:

$$B_B^{\times} + h^{\bullet} \leftrightarrow B_B^{\bullet} \qquad \Rightarrow \qquad K_{sph} = \frac{[B_B^{\bullet}]}{[B_B^{\times}]p} \tag{3.12}$$

Summing Eq.(3.11) and (3.12) gives:

$$2B_B^{\times} \leftrightarrow B_B' + B_B^{\bullet} \qquad \Rightarrow \qquad K_{spt} = \frac{[B_B^{\bullet}][B_B']}{[B_B^{\times}]^2} = \frac{[B_B']}{[B_B^{\times}]n} \cdot \frac{[B_B^{\bullet}]}{[B_B^{\times}]p} K_i = K_{spe} K_{sph} K_i \quad (3.13)$$

<u>*B*-site Mass Balance Equation ($B \equiv$ *Fe, Co)*</u>

$$[B_B^{\times}] + [B_B'] + [B_B^{\bullet}] = B_{tot} \quad (3.14)$$

Combining Eqs. (3.11) and (3.14) for $p <<< n$ yields:

$$[B_B^{\times}] + [B_B'] \approx B_{tot} \qquad \Rightarrow \qquad [B_B'] = \frac{nK_{spe}B_{tot}}{1 + nK_{spe}} \quad (3.15)$$

Combining Eqs. (3.12) and (3.14) for $n <<< p$ yields:

$$[B_B^{\times}] + [B_B^{\bullet}] \approx B_{tot} \qquad \Rightarrow \qquad [B_B^{\bullet}] = \frac{pK_{sph}B_{tot}}{1 + pK_{sph}} \quad (3.16)$$

Combining Eqs. (3.13) and (3.14) yields:

$$\begin{aligned} [B_B^{\bullet}] &= B_{tot} - \left(1 - \frac{1}{2K_{spt}}\right)[B_B'] \pm \frac{1}{2K_{spt}} \cdot \sqrt{\left(1 - 4K_{spt}\right)[B_B']^2 - 4K_{spt}[B_B']B_{tot}} \\ &= B_{tot} - \left(1 - \frac{1}{2K_{spe}K_{sph}K_i}\right)[B_B'] \pm \frac{\sqrt{\left(1 - 4K_{spe}K_{sph}K_i\right)[B_B']^2 - 4K_{spe}K_{sph}K_i[B_B']B_{tot}}}{2K_{spe}K_{sph}K_i} \end{aligned} \quad (3.17)$$

From analysis of Eqs. (3.13) and (3.14) in the region where $n \to 0$ and $p \to 0$ (i.e. $n << V$ and $p << V$), — similar to the analysis performed for K_D in SDC in Eqs. (2.5) to (2.11) — we can show that $K_{spe} = K_{sph} = 1/B_{tot}$. Substituting this expression into Eq. (3.17) gives:

$$[B_B^{\bullet}] = B_{tot} - \left(1 - \frac{B_{tot}^2}{2K_i}\right)[B_B'] \pm \frac{B_{tot}^2\sqrt{\left(1 - 4\frac{K_i}{B_{tot}^2}\right)[B_B']^2 - 4\frac{K_i}{B_{tot}}[B_B']}}{2K_i} \tag{3.18}$$

Also, to account for $n \geq [B_B^{\times}]$ or $p \geq [B_B^{\times}]$ we define

$$n = n_f + [B_B'] \tag{3.19}$$

and

$$p = p_f + [B_B^{\bullet}] \tag{3.20}$$

Finally, the <u>charge neutrality equation</u> for this system is given by

$$n + [Sr_{La}'] + 3[V_B'''] = 2[V_O^{\bullet\bullet}] + p \tag{3.21}$$

However in the typical *region of interest*, $[V_B'''] \approx 0$. Therefore the charge neutrality equation reduces to:

$$n + [Sr_{La}'] \approx 2[V_O^{\bullet\bullet}] + p \tag{3.22}$$

Eqs. (3.3) through (3.22) fully describe the defect equilibria of the LSCF MIEC. We can obtain expressions for the *region of interest* for this system by examining two limiting cases. First let us consider the *low* P_{O_2} region where p <<< $[Sr_{La}']$, $[V_O^{\bullet\bullet}]$, *n* and Eq. (3.22) becomes:

$$n + [Sr'_{La}] = 2[V_O^{\bullet\bullet}] \tag{3.23}$$

We can combine Eq. (3.23) with Eq. (3.3) as was done for SDC — Eqs. (2.14) to (2.20) — to get

$$V(P) = \left[\frac{1}{2} K_{R2}^{\frac{1}{2}} P^{-\frac{1}{4}} + \left(\frac{1}{2} [Sr'_{La}] \right)^{\frac{3}{2}} \right]^{\frac{2}{3}} \tag{3.24}$$

and

$$n(P) = K_{R2}^{\frac{1}{2}} P^{-\frac{1}{4}} \left[\frac{1}{2} K_{R2}^{\frac{1}{2}} P^{-\frac{1}{4}} + \left(\frac{1}{2} [Sr'_{La}] \right)^{\frac{3}{2}} \right]^{-\frac{1}{3}} \tag{3.25}$$

For the second case let us consider the *high* P_{O_2}, cathode, region where n <<< $[Sr'_{La}]$, $[V_O^{\bullet\bullet}]$, *p* and Eq. (3.22) becomes:

$$[Sr'_{La}] = 2[V_O^{\bullet\bullet}] + p \tag{3.26}$$

Eqs. (3.4) and (3.26) may be combined, as was done for bismuth oxide, to give a quadratic equation in terms of *V* or *p*. These equations each have one meaningful solution for *V* and *p* as follows:

$$V(P) = \frac{1}{16} \left[\left(K_{0x2} P^{\frac{1}{2}} + 8[Sr'_{La}] \right)^{\frac{1}{2}} - K_{0x2}^{\frac{1}{2}} P^{\frac{1}{4}} \right]^2 \tag{3.27}$$

and

$$p(P) = \frac{1}{4}\left(-K_{0x2}P^{\frac{1}{2}} + \sqrt{8[Sr'_{La}]K_{0x2}P^{\frac{1}{2}} + K_{0x2}^{2}P} \right) \tag{3.28}$$

SDC operates in the "*low* P_{O_2}" region — i.e., no holes are present at useful/typical partial pressures of oxygen — so Eqs. (2.19) and (2.20) give an adequate description of the defect concentration dependence on oxygen partial pressure. Similarly, bismuth oxide and cathodic LSCF operates in the "*high* P_{O_2}" region — i.e., no electrons are present at useful/typical partial pressures of oxygen — so Eqs. (3.1) (3.2), (3.27) and (3.28) likewise give sufficient description of the defect concentration dependence on oxygen partial pressure. However, for membrane applications, LSCF and other typical perovskite MIECs operate across regions in which both or either electrons or holes exist in non-negligible concentrations. Hence for a proper description of the vacancy concentration dependence on oxygen potential we must combine Eqs. (3.24) and (3.27) and since both expressions converge to $\frac{1}{2}[Sr'_{La}]$ at intermediate P_{O_2}, subtract $\frac{1}{2}[Sr'_{La}]$ to avoid duplication. Doing this and substituting A_p for $[Sr'_{La}]$ yields

$$V(P) = \frac{1}{16}\left[\left(K_{0x}P^{\frac{1}{2}} + 8A_p \right)^{\frac{1}{2}} - K_{0x}^{\frac{1}{2}}P^{\frac{1}{4}} \right]^2 + \left[\frac{1}{2}K_R^{\frac{1}{2}}P^{-\frac{1}{4}} + \left(\frac{1}{2}A_p\right)^{\frac{3}{2}} \right]^{\frac{2}{3}} - \frac{1}{2}A_p$$

(3.29)

Similarly for the concentration of holes we combine Eqs. (3.5), (3.7), (3.25) and (3.28) subtracting the term $K_{0x2}^{\frac{1}{2}}P^{\frac{1}{4}}\left(\frac{1}{2}A_p\right)^{\frac{1}{2}}$ to avoid duplication since both expressions converge to $K_{0x2}^{\frac{1}{2}}P^{\frac{1}{4}}\left(\frac{1}{2}A_p\right)^{\frac{1}{2}}$ at intermediate P_{O_2}. So doing yields:

$$p(P) = \frac{\sqrt{8A_pK_{0x2}P^{\frac{1}{2}} + K_{0x2}^{2}P} - K_{0x2}P^{\frac{1}{2}}}{4} + K_{0x2}^{\frac{1}{2}}P^{\frac{1}{4}}\left[\frac{K_{R2}^{\frac{1}{2}}P^{-\frac{1}{4}}}{2} + \left(\frac{A_p}{2}\right)^{\frac{3}{2}} \right]^{\frac{1}{3}} - K_{0x2}^{\frac{1}{2}}P^{\frac{1}{4}}\left(\frac{A_p}{2}\right)^{\frac{1}{2}}$$

Finally, for the concentration of electrons combine Eqs. (3.5), (3.7), (3.25) and (3.28) subtracting the term $K_{R2}^{\frac{1}{2}}\left(\frac{1}{2}A_p\right)^{-\frac{1}{2}}P^{-\frac{1}{4}}$ to avoid duplication since both expressions converge to $K_{R2}^{\frac{1}{2}}\left(\frac{1}{2}A_p\right)^{-\frac{1}{2}}P^{-\frac{1}{4}}$ at intermediate P_{O_2}. So doing yields:

$$n(P)=\frac{K_{R2}^{\frac{1}{2}}P^{-\frac{1}{4}}}{\left[\frac{1}{2}K_{R2}^{\frac{1}{2}}P^{-\frac{1}{4}}+\left(\frac{1}{2}A_p\right)^{\frac{3}{2}}\right]^{\frac{1}{3}}}+\frac{4K_{R2}^{\frac{1}{2}}K_{Ox2}^{\frac{1}{2}}}{-K_{Ox2}P^{\frac{1}{2}}+\sqrt{8A_pK_{Ox2}P^{\frac{1}{2}}+K_{Ox2}^2P}}-\frac{K_{R2}^{\frac{1}{2}}P^{-\frac{1}{4}}}{\left(\frac{1}{2}A_p\right)^{\frac{1}{2}}} \quad (3.31)$$

Eqs. (3.29) and (3.30) are plotted in Fig. 2.3 for arbritrarily chosen values of K_{Ox2} and K_{R2}. The form of the plots are consistent with experimental data and numerical solutions [11] of the defect equilibria.

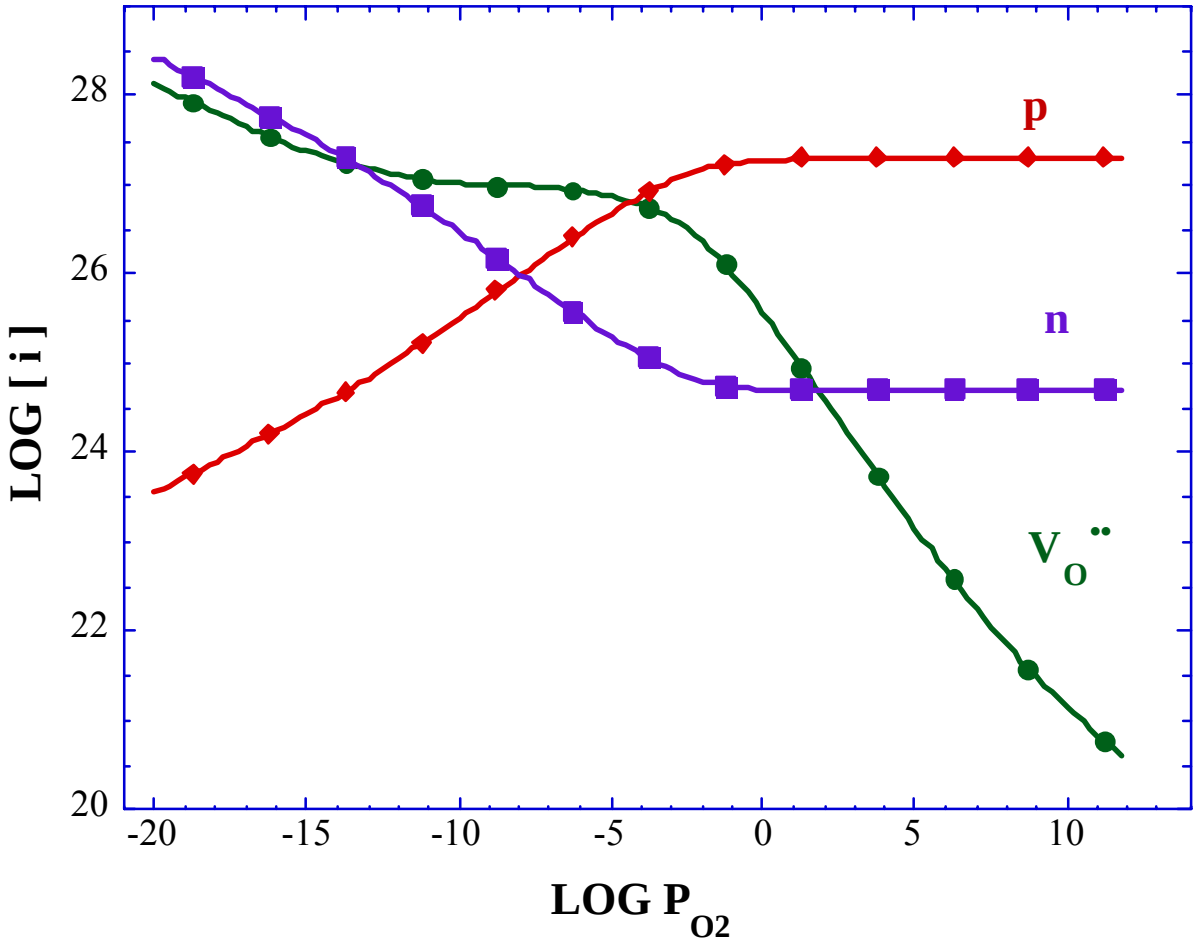

Figure 2.3 LSCF DED from the model for arbitrary values of K_{Ox2} and K_{R2}.

2.4 Defect Transport

Initially, in the manner of other researchers, we neglected to derive analytically the relationship between the electric field and the defect concentration gradients inside the MIEC. This has since been remedied and we have obtained such a relationship completely devoid of assumptions (save charge neutrality) and consistent with similar treatments in aqueous electrochemistry [12]. Before we tackle the issue of flux however, we will briefly review the work on conductivity so far.

2.4.1 Defect Conductivity and Ionic Transference Number as Functions of Pressure

Having earlier derived expressions for the functional dependence of defect concentrations on oxygen potential in an MIEC [2] — reviewed in **Section 2.2** — we may now obtain expressions for the defect conductivity and ionic transference number of an MIEC. The conductivity of the MIEC with respect to vacancies, electrons and holes is given by:

$$\sigma_V(P) = |z_V| F u_V V(P) \tag{4.1}$$

$$\sigma_e(P) = |z_e| F u_e n(P) \tag{4.2}$$

$$\sigma_h(P) = |z_h| F u_h p(P) \tag{4.3}$$

where z is the charge equivalence, u is the mobility, F is Faradays constant and the subscripts V, e, and h refer to the defect type, i.e., vacancies electrons and holes respectively. To get the conductivity of an MIEC we substitute the appropriate expressions for $V(P)$ $n(P)$ and $p(P)$ from Eqs. (2.19), (2.20), (3.1), (3.2) (3.29), (3.30), and (3.31). The total conductivity, σ_{tot}, of an MIEC is the sum of the conductivities of all the charge carriers and is given by the sum of Eqs (4.1), (4.2) and (4.3):

$$\sigma_{tot}(P) = \sigma_V(P) + \sigma_e(P) + \sigma_h(P) = |z_V| F u_V V(P) + |z_e| F u_e n(P) + |z_h| F u_h p(P) \tag{4.4}$$

The ionic transference number t_i is defined as the ratio of the ionic conductivity (which is σ_V for the oxide MIECs of interest) to the total conductivity and is given by:

$$t_i = \frac{\sigma_V}{\sigma_{tot}} = \frac{|z_V| F u_V V(P)}{|z_V| F u_V V(P) + |z_e| F u_e n(P) + |z_h| F u_h p(P)} \tag{4.5}$$

When Eqs. (4.4) and (4.5) are fitted to experimental data [7] as in Fig. 2.4, an excellent/ideal fit is obtained. This is done by using a value of u_V obtained from experimental data [7] and varying the vales of u_e and K_R to get the best fit. However, we found that there is a unique u_e for each K_R selected within a certain range of K_R values and *vice-versa*. This situation is not satisfactory and thus we need to find a way to determine experimentally the values of at least one of u_e or K_R . This is not a trivial matter however, because, as reviewed recently by Steele [13], the usual experimental procedures are fraught with error . Especially with regards to electrode overpotentials. Nonetheless, we have devised a few techniques, which will be discussed in **Section 2.5**, that we think will yield better results than obtained in the past.

2.4.2 Defect Flux

Given, η_k is the electrochemical potential, μ_k is the chemical potential, c_k is the concentration and D_k is the diffusivity of the kth defect; and Φ is potential, the flux of the kth defect is given by:

$$j_k = -\frac{\sigma_k}{z_k^2 F^2} \nabla \eta_k = -\frac{\sigma_k}{z_k^2 F^2} \left(\nabla \mu_k + z_k F \nabla \Phi \right) = -D_k \nabla c_k - z_k c_k D_k \frac{F}{RT} \nabla \Phi$$

(4.6)

where

$$\sigma_k = z_k F u_k c_k = \frac{z_k^2 F^2 c_k D_k}{RT} \tag{4.7}$$

and

$$u_k = \frac{z_k F D_k}{RT} \tag{4.8}$$

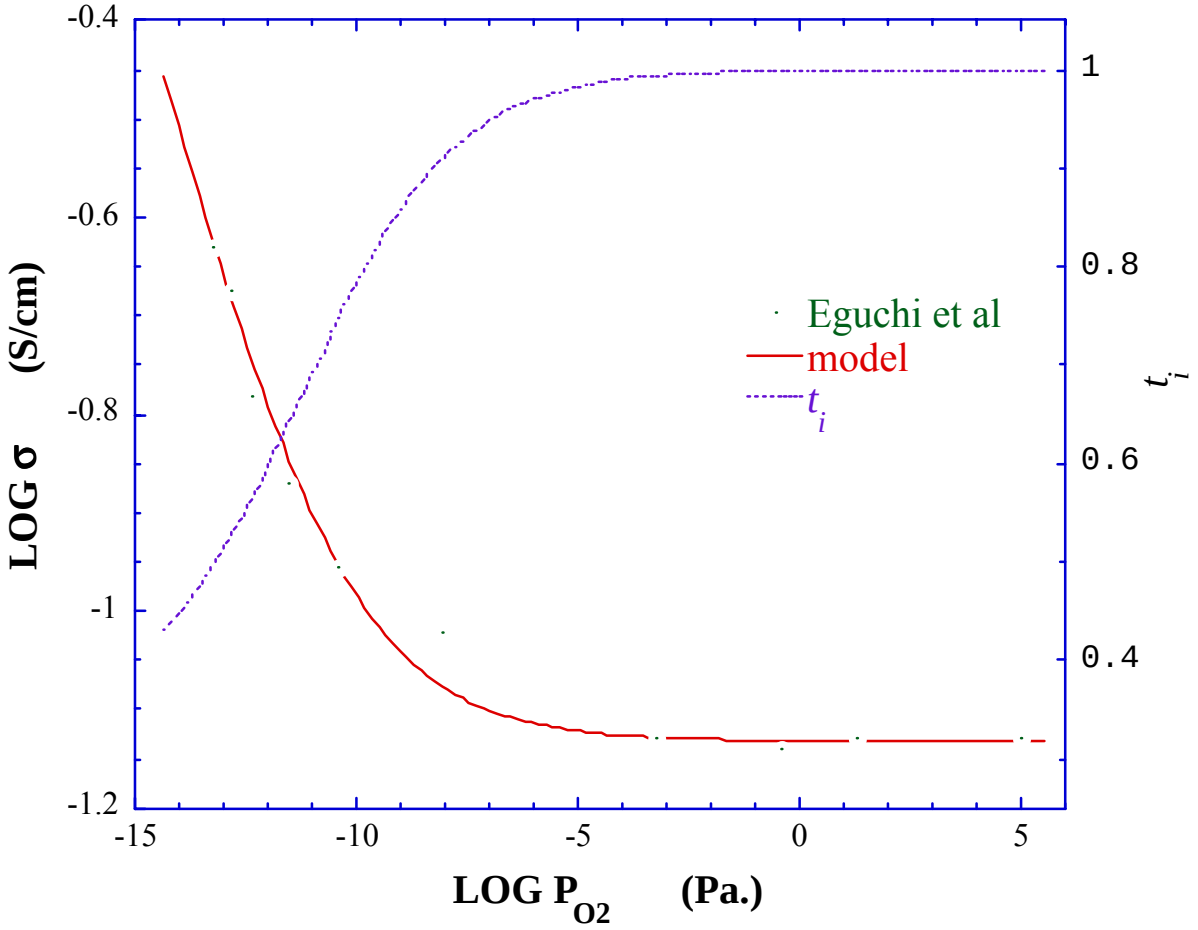

Figure 2.4 Conductivity equation, σ(P), derived from the model and fitted to data from Eguchi *et al* [7] for SDC.

Eq. (4.6) contains two variables namely the concentration and the potential gradient. In the preceding sections we have obtained expressions for the defect concentrations and can, in principle, obtain the concentration gradients from those expressions. However, we have yet to obtain an expression for the potential gradient. Typically, researchers have assumed this to be a constant however we would like to explicitly define the potential. This may be achieved by considering that for defects diffusing through an MIEC no charge accumulation occurs at steady state. Thus, in the absence of homogenous reactions between the defects, the fluxes are related by the charge balance:

$$2j_V + j_h = j_e \tag{4.9}$$

By combining Eqs. (4.6) and (4.9) for the relevant defects we can obtain an expression for the potential in terms of the concentration gradients as follows:

$$2D_V\nabla V + 2z_V D_V V\frac{F}{RT}\nabla\Phi + D_h\nabla p + z_h D_h p\frac{F}{RT}\nabla\Phi = D_e\nabla n + z_e D_e n\frac{F}{RT}\nabla\Phi$$

Rearranging we have:

$$\frac{F}{RT}\nabla\Phi\left(2z_V D_V V + z_h D_h p - z_e D_e n\right) = D_e\nabla n - 2D_V\nabla V - D_h\nabla p \tag{4.10}$$

or

$$\nabla\Phi = \frac{RT}{F}\cdot\frac{D_e\nabla n - 2D_V\nabla V - D_h\nabla p}{2z_V D_V V + z_h D_h p - z_e D_e n} = \frac{RT}{F}\cdot\frac{D_e n\nabla\mu_e - 2D_V V\nabla\mu_V - D_h p\nabla\mu_h}{2z_V D_V V + z_h D_h p - z_e D_e n} \tag{4.11}$$

In Eq. (4.11) we have an explicit relationship between the potential and the concentration and chemical potential gradients; the concentrations and the diffusivities of the defects. Substituting Eqs. (4.2) and (4.11) into Eq. (4.6) for each defect yields

$$\begin{aligned} j_V &= -D_V\nabla V - z_V V D_V\frac{F}{RT}\nabla\Phi \\ &= -D_V\frac{\left(z_h D_h p - z_e D_e n\right)\nabla V + z_V V\left(D_e\nabla n - D_h\nabla p\right)}{2z_V D_V V - z_e D_e n + z_h D_h p} \\ &= -D_V\frac{\left(\frac{\sigma_h}{z_h} - \frac{\sigma_e}{z_e}\right)\nabla V + \frac{\sigma_V}{z_V D_V}\left(D_e\nabla n - D_h\nabla p\right)}{2\frac{\sigma_V}{z_V} - \frac{\sigma_e}{z_e} + \frac{\sigma_h}{z_h}} \\ &= -\frac{2\left(\sigma_h + \sigma_e\right)D_V\nabla V + \sigma_V\left(D_e\nabla n - D_h\nabla p\right)}{2\sigma_{tot}} \end{aligned} \tag{4.12}$$

$$j_e = -D_e\nabla n - z_e n D_e\frac{F}{RT}\nabla\Phi$$

$$
\begin{aligned}
&= -D_e \frac{\left(2z_V D_V V + z_h D_h p\right)\nabla n - z_e n\left(2D_V \nabla V + D_h \nabla p\right)}{2z_V D_V V + z_h D_h p - z_e D_e n} \\
&= -D_e \frac{\left(2\frac{\sigma_V}{z_V} + \frac{\sigma_h}{z_h}\right)\nabla n - \frac{\sigma_e}{z_e D_e}\left(2D_V \nabla V + D_h \nabla p\right)}{2\frac{\sigma_V}{z_V} + \frac{\sigma_h}{z_h} - \frac{\sigma_e}{z_e}} \\
&= -\frac{\left(\sigma_V + \sigma_h\right)D_e \nabla n + \sigma_e\left(2D_V \nabla V + D_h \nabla p\right)}{\sigma_{tot}}
\end{aligned}
\tag{4.13}
$$

$$
\begin{aligned}
j_h &= -D_h \nabla p - z_h p D_h \frac{F}{RT}\nabla \Phi \\
&= -D_h \frac{\left(2z_V D_V V - z_e D_e n\right)\nabla p + z_h p\left(D_e \nabla n - 2D_V \nabla V\right)}{2z_V D_V V + z_h D_h p - z_e D_e n} \\
&= -D_h \frac{\left(2\frac{\sigma_V}{z_V} - \frac{\sigma_e}{z_e}\right)\nabla p + \frac{\sigma_h}{z_h D_h}\left(D_e \nabla n - 2D_V \nabla V\right)}{2\frac{\sigma_V}{z_V} + \frac{\sigma_h}{z_h} - \frac{\sigma_e}{z_e}} \\
&= -\frac{\left(\sigma_V + \sigma_e\right)D_h \nabla p + \sigma_h\left(D_e \nabla n - 2D_V \nabla V\right)}{\sigma_{tot}}
\end{aligned}
\tag{4.14}
$$

Thus far we have not been very careful in defining what the conductivity of a species means in a concentration gradient. Eqs. (4.1) to (4.4) define the conductivity of a defect species as a function of a single oxygen partial pressure value for which there exists a single concentration. However, in a oxygen potential gradient — i.e., a concentration gradient — the conductivity is not the same everywhere inside the MIEC. Therefore, we must replace the conductivities in all the flux equations by an effective conductivity (to be denoted by an "*eff*" subscript) that will represent the measurable conductivity of the MIEC.

Evaluating the effective conductivity of the electrolyte requires the summation of the defect conductivities at every *i*th point (in one dimension) in the electrolyte. Therefore, the effective conductivity of the *k*th defect species, $\sigma_{k_{eff}}$ in the partial pressure gradient, may be determined by considering the electrolyte as a series arrangement of infinitesimally small slices of the material of identical cross-sectional area, *S*. The effective conductance $G_{k_{eff}}$ of such an arrangement is given by:

$$\frac{1}{G_{k_{eff}}} = \sum_{i=1}^{N} \frac{1}{G_{k_i}} \tag{4.15}$$

where N is the number of *slices* and $N = L/l$ (l is the average thickness of each individual *slice*). In terms of conductivity, the effective conductance is given by

$$G_{k_{eff}} = \frac{\sigma_{k_{eff}} S}{L} \tag{4.16}$$

Similarly for the conductance of the *i*th *slice*

$$G_{k_i} = \frac{\sigma_{k_i} S}{l} = \frac{\sigma_{k_i} S}{\Delta x} \tag{4.17}$$

where $l = \Delta x$. These definitions allow Eq. (4.15) to be rewritten as

$$\frac{L}{\sigma_{k_{eff}} S} = \sum_{i=1}^{N} \frac{\Delta x}{\sigma_{k_i} S} \tag{4.18}$$

or

$$\frac{1}{\sigma_{k_{eff}}} = \sum_{i=1}^{N} \frac{1}{\sigma_{k_i}} \cdot \frac{\Delta x}{L} \tag{4.19}$$

Therefore, for a large number of equally thin slices each of thickness, such that $\Delta x \rightarrow dx$, one may write

$$\frac{1}{\sigma_{k_{eff}}} = \frac{1}{L}\int_0^L \frac{1}{\sigma_k(x)} dx \tag{4.20}$$

Additionally, Eq. (2.23) may be differentiated to yield:

$$\frac{dx}{L} = \frac{d(\ln P)}{\ln P_L - \ln P_0} = \frac{dP}{P}\frac{1}{\ln P_L - \ln P_0} \tag{4.21}$$

which may be substituted into Eq. (4.20) to give:

$$\frac{1}{\sigma_{k_{eff}}} = \frac{1}{L}\int_0^L \frac{1}{\sigma_k(x)} \cdot dx = \frac{1}{\ln P_L - \ln P_0}\int_{P_0}^{P_L} \frac{1}{\sigma_k(P)} \cdot \frac{dP}{P} \tag{4.22}$$

or

$$\frac{1}{\sigma_{k_{eff}}} = \frac{1}{L}\int_0^L \frac{1}{\sigma_k} \cdot dx = \frac{1}{L}\int_0^L \frac{1}{|z_k| F u_k[k]} \cdot dx = \frac{1}{\ln P_L - \ln P_0}\int_{P_0}^{P_L} \frac{1}{|z_k| F u_k[k]} \cdot \frac{dP}{P} \tag{4.23}$$

Hence, for the effective conductivity of vacancies, electrons and holes we have:

$$\sigma_{V_{eff}} = |z_V| F u_V \left(\frac{1}{L}\int_0^L \frac{1}{V(x)} \cdot dx\right)^{-1} = |z_V| F u_V V_{eff} \tag{4.24}$$

$$\sigma_{e_{eff}} = |z_e| F u_e \left(\frac{1}{L}\int_0^L \frac{1}{n(x)} \cdot dx\right)^{-1} = |z_e| F u_e n_{eff} \tag{4.25}$$

$$\sigma_{h_{eff}} = |z_h| F u_h \left(\frac{1}{L}\int_0^L \frac{1}{V(x)} \cdot dx\right)^{-1} = |z_h| F u_h p_{eff} \tag{4.26}$$

And for the flux of vacancies, electrons and holes we have:

$$j_V = -\frac{2\left(\sigma_{h_{eff}} + \sigma_{e_{eff}}\right) D_V \nabla V + \sigma_{V_{eff}}\left(D_e \nabla n - D_h \nabla p\right)}{2\sigma_{tot_{eff}}} \tag{4.27}$$

$$j_e = -\frac{\left(\sigma_{V_{eff}} + \sigma_{h_{eff}}\right) D_e \nabla n + \sigma_{e_{eff}}\left(2D_V \nabla V + D_h \nabla p\right)}{\sigma_{tot_{eff}}} \tag{4.28}$$

$$j_h = -\frac{\left(\sigma_{V_{eff}} + \sigma_{e_{eff}}\right) D_h \nabla p + \sigma_{h_{eff}}\left(D_e \nabla n - 2D_V \nabla V\right)}{\sigma_{tot_{eff}}} \tag{4.29}$$

Finally, since the flux at steady state is a constant (i.e., with neither charge accumulation nor homogenous reactions present) then the concentration gradients — the only remaining "variables" — must also be constant. To resolve this we would like to use the principle of *independence of path* — i.e., a charge/particle moving in a frictionless field from point A to point B dissipates the same energy irrespective of the path it takes from A to B — in the flux equations. By this principle we can now use one gradient to represent the actual diffusion path taken by a diffusing defect. That gradient is the average gradient and is given for the *k*th defect by:

$$average\,\nabla[k] = \frac{1}{L}\int_0^L \nabla[k]\cdot dx = \frac{1}{L}\int_0^L \frac{d[k]}{dx}\cdot dx = \frac{1}{L}\int_{[k]_0}^{[k]_L} d[k] = \frac{[k]_L - [k]_0}{L} \tag{4.30}$$

Incorporating Eq.(4.30) into Eqs. (4.27) to (4.29) for the defect fluxes yields:

$$\begin{aligned} j_V &= -\frac{2\left(\sigma_{e_{eff}} + \sigma_{h_{eff}}\right) D_V \Delta V + \sigma_{V_{eff}}\left(D_e \Delta n - D_h \Delta p\right)}{2\sigma_{tot_{eff}} L} \\ &= -D_V\left(t_{e_{eff}} + t_{h_{eff}}\right)\frac{\Delta V}{L} - t_{i_{eff}}\frac{\left(D_e \Delta n - D_h \Delta p\right)}{2L} \end{aligned} \tag{4.31}$$

$$j_e = -\frac{\left(\sigma_{V_{eff}} + \sigma_{h_{eff}}\right) D_e \Delta n + \sigma_{e_{eff}} \left(2D_V \Delta V + D_h \Delta p\right)}{\sigma_{tot_{eff}} L}$$

$$= -\left(t_{i_{eff}} + t_{h_{eff}}\right) D_e \frac{\Delta n}{L} - t_{e_{eff}} \frac{\left(2D_V \Delta V + D_h \Delta p\right)}{L} \tag{4.32}$$

$$j_h = -\frac{\left(\sigma_{V_{eff}} + \sigma_{e_{eff}}\right) D_h \Delta p + \sigma_{h_{eff}} \left(D_e \Delta n - 2D_V \Delta V\right)}{\sigma_{tot_{eff}} L}$$

$$= -\left(t_{i_{eff}} + t_{e_{eff}}\right) D_h \frac{\Delta p}{L} - t_{h_{eff}} \frac{\left(D_e \Delta n - 2D_V \Delta V\right)}{L} \tag{4.33}$$

where $\Delta V = V_L - V_0$, $\Delta n = n_L - n_0$, $\Delta p = p_L - p_0$ — the subscripts refer to the values at $x = 0$ and $x = L$ — and

$$t_{i_{eff}} = \frac{\sigma_{V_{eff}}}{\sigma_{tot_{eff}}} \tag{4.34}$$

$$t_{e_{eff}} = \frac{\sigma_{e_{eff}}}{\sigma_{tot_{eff}}} \tag{4.35}$$

$$t_{h_{eff}} = \frac{\sigma_{h_{eff}}}{\sigma_{tot_{eff}}} \tag{4.36}$$

2.4.3 Oxygen Flux

Since the oxygen flux is directly related to the flux of defects and is also relevant to determining the properties of an MIEC and later a bilayer, we would like to determine the functional dependence of the flux of oxygen on the defect transport properties. The oxygen flux through an MIEC is given by:

$$j_{O_2} = -\frac{1}{4^2F^2}\frac{\sigma_{V_{eff}}\left(\sigma_{e_{eff}}+\sigma_{h_{eff}}\right)}{\sigma_{tot_{eff}}}\nabla\mu_{O_2} = -\frac{\nabla\mu_{O_2}}{4^2F^2}\left(\frac{\sigma_{V_{eff}}\sigma_{e_{eff}}}{\sigma_{tot_{eff}}}+\frac{\sigma_{V_{eff}}\sigma_{h_{eff}}}{\sigma_{tot_{eff}}}\right) \quad (4.37)$$

If we assume that the internal defect chemical reactions are not disturbed by defect transport, the chemical potential gradients of individual charged species can be converted into the virtual chemical potential of gaseous oxygen. In other words, at equilibrium we can rewrite Eqs. (3.3) and (3.4) as follows:

$$0 = \nabla\mu_V + 2\nabla\mu_e + \tfrac{1}{2}\nabla\mu_{O_2} = \nabla\eta_V + 2\nabla\eta_e + \tfrac{1}{2}\nabla\mu_{O_2} \quad (4.38)$$

and

$$0 = \nabla\mu_V + \tfrac{1}{2}\nabla\mu_{O_2} - 2\nabla\mu_h = \nabla\eta_V + \tfrac{1}{2}\nabla\mu_{O_2} - 2\nabla\eta_h \quad (4.39)$$

We are also assuming that the chemical potential of the lattice oxygen $\mu_{O_O^\times}$ is a constant. This isn't wholly true since the vacancy concentration is tied to the concentration of lattice oxygen through the site exclusion effect. It is, however, a safe assumption for dilute electrolytes where the vacancy concentration is much smaller than the concentration of lattice oxygen.

Combining Eqs. (4.5), (4.6), (4.37), (4.38) and (4.39) we get:

$$\begin{aligned} j_{O_2} &= \frac{1}{4^2F^2}\left[\frac{\sigma_{V_{eff}}\sigma_{e_{eff}}}{\sigma_{tot_{eff}}}\left(2\nabla\eta_V + 4\nabla\eta_e\right) - \frac{\sigma_{V_{eff}}\sigma_{h_{eff}}}{\sigma_{tot_{eff}}}\left(-2\nabla\eta_V + 4\nabla\eta_h\right)\right] \\ &= \frac{1}{8F^2}\left[\frac{z_V^2F^2\left(\sigma_{e_{eff}}+\sigma_{h_{eff}}\right)}{\sigma_{tot_{eff}}}\frac{\sigma_{V_{eff}}}{z_V^2F^2}\nabla\eta_V + \frac{2z_e^2F^2\sigma_{V_{eff}}}{\sigma_{tot_{eff}}}\frac{\sigma_{e_{eff}}}{z_e^2F^2}\nabla\eta_e - \frac{2z_h^2F^2\sigma_{V_{eff}}}{\sigma_{tot_{eff}}}\frac{\sigma_{h_{eff}}}{z_h^2F^2}\nabla\eta_h\right] \\ &= \frac{1}{8}\left[-z_V^2\left(t_{e_{eff}}+t_{h_{eff}}\right)j_V - 2z_e^2t_{i_{eff}}j_e + 2z_h^2t_{i_{eff}}j_h\right] \end{aligned} \quad (4.40)$$

2.5 Experimental Considerations: Determining u_e and K_R

In an attempt to improve the quantitative capabilities of the model as well as to verify its overall soundness, we fitted the model to the experimental data of Eguchi *et al* [7] we were able to get excellent fits to their data however two important parameters u_e and K_R had to be estimated/"fitted" to achieve the best fit. Additionally, u_e and K_R are co-dependent — i.e., changing one changes the other (there is a unique u_e for each K_R). Hence, one cannot use any of the values of u_e and K_R so obtained, independently. To solve this dilemma we will propose a few ways of determining the value of u_e and K_R. We will be limiting our discussion to *n*-type MIECs such as SDC, however, all experiments developed in the following sections are applicable to *p*-type MIECs as well.

2.5.1 Determining u_e

2.5.1.1 Using the Effective Ionic Transference Number $\bar{t}_i$ (i.e., t_i Measured in a P_{O_2} Gradient)

In this section we propose to make use of the effective ionic transference number $\bar{t}_i$ defined in Eq. (4.34) because at least in principle it is experimentally very accessible. If we combine Eqs. (4.7) and (4.34) we get:

$$\bar{t}_i = \frac{\sigma_{V_{eff}}}{\sigma_{V_{eff}} + \sigma_{e_{eff}}} = \frac{z_V^2 V_{eff} D_V}{z_V^2 V_{eff} D_V + z_e^2 n_{eff} D_e} \tag{5.1}$$

In the low P_{O_2} range, where $n = 2V$ Eq. (5.1) becomes:

$$\bar{t}_i = \frac{z_V^2 D_V}{z_V^2 D_V + 2 z_e^2 D_e} \tag{5.2}$$

Since

$$\bar{t}_i = \frac{\Phi_{oc}}{\Phi_{th}} \tag{5.3}$$

where Φ_{oc} is the open circuit potential and Φ_{th} is the Nernst potential, then Eq. (5.2) may be rewritten as follows:

$$D_e = \frac{z_V^2 D_V - \bar{t}_i z_V^2 D_V}{2\bar{t}_i z_e^2} = \frac{z_V^2 D_V}{2z_e^2}\left(\frac{1}{\bar{t}_i} - 1\right) = 2D_V\left(\frac{1}{\bar{t}_i} - 1\right) = 2D_V\left(\frac{\Phi_{th}}{\Phi_{oc}} - 1\right) \qquad (5.4)$$

or, by combining Eqs. (4.8) and (5.2), as

$$u_e = \frac{|z_V|}{2|z_e|}u_V\left(\frac{1}{\bar{t}_i} - 1\right) = u_V\left(\frac{1}{\bar{t}_i} - 1\right) = u_V\left(\frac{\Phi_{th}}{\Phi_{oc}} - 1\right) \qquad (5.5)$$

Φ_{th} may be calculated from the Nernst Equation. D_V or u_V may be determined from **ln** σT vs. 1/T plots for the MIEC at a suitable oxygen partial pressures so that it is in its electrolytic region. Finally, Φ_{oc} may be obtained from voltage measurements.

The most difficult source of error to eliminate or minimize for an experiment based on Eqs. (5.4) or (5.5) comes from the electrodic overpotentials present during a measurement of Φ_{oc} . This is potentially a major problem, however recent studies by Gödickemeier *et al* [14, 15] may help in the quantification of said overpotentials. Conversely, the strength of this approach lies in its simplicity since ideally the only apparatus required beyond the fuel cell setup — which itself may be arduous — is a good voltmeter.

2.5.1.2 Using Simultaneous Conductivity and j_{O_2} measurements in a P_{O_2} Gradient

Another possible approach to determining u_e and K_R is to perform simultaneous measurements of oxygen diffusion flux, j_{O_2} , and conductivity in a P_{O_2} gradient. This is outlined in the following development.

Given that

$$\mu_{O_2} = RT\ln P_{O_2} \qquad (5.6)$$

We may combine Eqs. (4.7) and (4.37) to get:

$$j_{O_2} = -\frac{\nabla \ln P_{O_2}}{4^2} \cdot \frac{z_V^2 z_e^2 V_{eff} n_{eff} D_V D_e}{z_V^2 V_{eff} D_V + z_e^2 n_{eff} D_e} \tag{5.7}$$

at oxygen partial pressures where $n = 2V$ ($P_{O_2} \leq \sim 10^{-18}$ atm. for SDC, see Fig. 1) Eq. (5.7) becomes:

$$j_{O_2} = -\frac{\nabla \ln P_{O_2}}{4^2} \cdot \frac{2 z_V^2 z_e^2 D_V D_e}{z_V^2 D_V + 2 z_e^2 D_e} V_{eff} \tag{5.8}$$

Similarly Eq. (4.11) combined with Eq. (4.7) gives:

$$\sigma_{tot_{eff}} = z_V^2 F^2 V_{eff} \frac{D_V}{RT} + z_e^2 F^2 n_{eff} \frac{D_e}{RT} \tag{5.9}$$

and at oxygen partial pressures where $n = 2V$, it reduces to:

$$\sigma_{tot_{eff}} = \frac{F^2 V_{eff}}{RT} \left(z_V^2 D_V + 2 z_e^2 D_e \right) \tag{5.10}$$

Dividing Eq. (5.8) by (5.10) we get for the region where $n = 2V$

$$\frac{j_{O_2}}{\sigma_{tot_{eff}}} = -\frac{RT \nabla \ln P_{O_2}}{4^2 F^2} \cdot \frac{2 z_V^2 z_e^2 D_V D_e}{\left(z_V^2 D_V + 2 z_e^2 D_e \right)^2} = -\frac{RT \nabla \ln P_{O_2}}{2F^2} \cdot \frac{D_V D_e}{4\left(2D_V + D_e \right)^2} \tag{5.11}$$

If we define

$$\gamma = \frac{-8 j_{O_2} F^2}{\sigma_{tot_{eff}} RT \nabla \ln P_{O_2}} = \frac{D_V D_e}{\left(2D_V + D_e\right)^2} \tag{5.12}$$

then we may rewrite Eq. (5.11) as follows

$$0 = \gamma D_e^2 + (4\gamma - 1) D_V D_e + 4\gamma D_V^2 \tag{5.13}$$

Eq. (5.13) when correctly analyzed has one meaningful unambiguous solution, given by:

$$D_e = \frac{(1 - 4\gamma) D_V - \sqrt{(4\gamma - 1)^2 D_V^2 - 16\gamma^2 D_V^2}}{2\gamma} = \frac{1 - 4\gamma - \sqrt{1 - 8\gamma}}{2\gamma} D_V \tag{5.14}$$

The terms comprising γ are experimentally accessible. The oxygen flux may be obtained from a mass spectrometer or oxygen sensor and $\sigma_{tot_{eff}}$ from an AC impedance analyzer. Primary difficulties may include low flux readings caused by the small P_{O_2} gradient necessitated by the requirement of remaining completely in the reducing region (i.e., at oxygen partial pressures where $n = 2V$). A low oxygen flux may test the sensitivity and reproducibility limits of the detecting instrument(s) — e.g., mass spectrometer or oxygen sensor. Another major difficulty arises from the desire to perform the experiments simultaneously. Though not absolutely necessary, it would be best in order to avoid the problems of reproducibility.

2.5.2 Determining K_R

2.5.2.1 Thermodynamics

Here what we are after is the value of K_R from Eq. (2.15). Some sense of the approximate value of K_R may be deduced by considering the transformation of Cerium (IV) Oxide to Cerium (III) Oxide which may be written as

$$2CeO_2 \leftrightarrow Ce_2O_3 + \tfrac{1}{2}O_2 \tag{5.15}$$

with the corresponding equilibrium constant for the transformation, K_{Tr}, given by

$$K_{Tr} = \frac{a_{Ce_2O_3} a_{O_2}^{\frac{1}{2}}}{a_{CeO_2}^2} = \exp\left(-\frac{\Delta G_{Tr}}{RT}\right) \tag{5.16}$$

However, since we can represent ceria as:

$$CeO_2 \equiv Ce_{Ce}^{\times} + 2O_O^{\times} \tag{5.17}$$

Then, as a **first approximation**, Eq. (5.15) may be rewritten as:

$$2Ce_{Ce}^{\times} + 4O_O^{\times} \leftrightarrow 2Ce'_{Ce} + 3O_O^{\times} + V_O^{\bullet\bullet} + \tfrac{1}{2}O_2 \tag{5.18}$$

with the corresponding equilibrium constant for the reaction in Eq. (5.18), K'_{Tr}, given by

$$K'_{Tr} = \frac{[Ce'_{Ce}]^2[O_O^{\times}]^3[V_O^{\bullet\bullet}]\left(P/P_{ref}\right)^{\frac{1}{2}}}{[Ce_{Ce}^{\times}]^2[O_O^{\times}]^4} = \frac{[Ce'_{Ce}]^2[V_O^{\bullet\bullet}]\left(P/P_{ref}\right)^{\frac{1}{2}}}{[Ce_{Ce}^{\times}]^2[O_O^{\times}]} = \exp\left(-\frac{\Delta G'_{Tr}}{RT}\right) \tag{5.19}$$

Where $\Delta G'_{Tr}$ includes the enthalpy of vacancy formation and the entropy change in the ceria lattice.

It is unlikely that Eqs. (5.15) and (5.18) are truly equivalent since we can expect that $\Delta G'_{Tr}$ is not equal to ΔG_{Tr} because $\Delta G'_{Tr}$ includes a large and favourable (positive) contribution from the configurational entropy arising from the comparatively large defect population. Whereas for ΔG_{Tr} there is at least a smaller contribution from the configurational entropy since Ce_2O_3 has a significantly lower defect population than $CeO_{2-\delta}$. Effectively, the transformation of $CeO_{2-\delta}$ to

ordered Ce_2O_3 eliminates the vacancies that existed in the disordered $CeO_{2-\delta}$. It is difficult however to speculate what the relative magnitude of enthalpy contributions for the respective reactions

Therefore we may write:

$$\Delta G'_{Tr} = \Delta G_{Tr} + RT \ln\theta \tag{5.20}$$

and

$$K'_{Tr} = K_{Tr} \times \theta \qquad \theta > 0 \tag{5.21}$$

where θ is a dimensionless correction term to account for the free energy difference between the transformation of CeO_2 to $CeO_{2-\delta}$ and CeO_2 to Ce_2O_3. Hence, combining Eqs. (2.15), (5.16), (5.19) and (5.21) — for $n < [Ce_{Ce}^{\times}]$ such that $n \equiv [Ce'_{Ce}]$ — yields:

$$K_{Tr} \times \theta = \frac{K_R \left(P_{ref}\right)^{-\frac{1}{2}}}{[Ce_{Ce}^{\times}]^2 [O_O^{\times}]} \tag{5.22}$$

K_R may now be deduced by substituting values for P_{ref}, $[Ce_{Ce}^{\times}]$, $[O_O^{\times}]$ and K_{Tr} which may be obtained from thermodynamic tables. Consequently, for $P_{ref} = 1$ atm, $[Ce_{Ce}^{\times}] \approx 2\text{x}10^{28}$ m^{-3} (SDC lattice constant = 0.544 nm [16] and doping ceria with 10 mol% Sm_2O_3 results in 20% of the cation sites being $[Sm'_{Ce}]$) $[O_O^{\times}] \approx 4.75\text{x}10^{28}$ m^{-3} (doping ceria with 10 mol% Sm_2O_3 results in 5% of the anion sites being vacant) and $K_{Tr} = 10^{-11.13}$ (at 1100 K) we obtain $K_R / \theta = 10^{74.1}$ m^{-9}atm.$^{1/2}$ or $\log K_R = 74.1 + \log\theta$. Without a more rigorous thermodynamic analysis it is difficult to ascertain the true magnitude of θ, but at the very least this calculation of K_R should give some confidence that the value deduced from fitting Eq. (4.4) to experimental data is reasonable.

2.5.2.2 From Dielectric Constant Measurements

At the frequencies used for AC impedance measurements (100 Hz to 1 MHz) the dielectric properties of a typical oxide MIEC is dominated by either ionic polarization or dipolar ("ion jump") polarization — the latter being the most dominant if it is present. The polarization mechanism can be distinguished by investigating the temperature dependence of the dielectric constant in a separate experiment. If the dielectric constant is relatively temperature insensitive then we may safely assume that the dielectric behaviour is governed by ionic polarization. Conversely, if the dielectric constant is inversely proportional to temperature we can deduce that it is due to dipolar polarization.

Both polarization mechanisms depend on the number of ions and ion pairs per unit volume. And the number of ions and ion pairs depend on the number of cations and anions (i.e., the number of filled cation and anion sites) present. Hence a change in the concentration of vacancies — say due to pressure at constant temperature — should change the dielectric constant of the material. If this change is detectable by AC impedance spectroscopy the we would be able to relate the change in the dielectric constant to the concentration of vacancies in the MIEC.

We will now develop the general approach for an MIEC such as SDC assuming that the dielectric properties are dominated by ionic polarization.

The dielectric constant of a material, k, may be expressed as a complex quantity

$$k = k' - ik'' \tag{5.23}$$

If the dominant mode of polarization is ionic polarization then

$$k'_{ion}(\omega) = 1 + \frac{z_{cation} z_{anion} e^2 N_{ion} \left(\omega_{ion}^2 - \omega^2\right)}{\varepsilon_0 M_{red} \left[\left(\omega_{ion}^2 - \omega^2\right)^2 + f_{ion}^2 \omega^2\right]} \tag{5.24}$$

and

$$k''_{ion}(\omega) = \frac{z_{cation} z_{anion} e^2 N_{ion} f_{ion} \omega}{\varepsilon_0 M_{red} \left[\left(\omega_{ion}^2 - \omega^2 \right)^2 + f_{ion}^2 \omega^2 \right]} \tag{5.25}$$

where

$$M_{red} = \frac{m_{cation} m_{anion}}{m_{cation} + m_{anion}} \tag{5.26}$$

N_{ion} is the number of ion pairs (cation-anion), f_{ion} is the damping constant, ω_{ion} is the natural frequency of vibration, M_{red} is the relative mass, m_{cation} and m_{anion} are the masses of the cation and anion respectively and z_{cation} and z_{anion} are the charge equivalents of the cation and anion respectively.

The number of ion pairs and their reduced masses will be affected by the creation of vacancies which will modify Eqs. (5.24) to (5.26) as shown below:

$$k'_{ion}(\omega) = 1 + \frac{z_{cation} z_{anion} e^2 \left(1 - X_V(T,P)\right) N_{ion} \left(\omega_{ion}^2 - \omega^2 \right)}{\varepsilon_0 M'_{red}(T,P) \left[\left(\omega_{ion}^2 - \omega^2 \right)^2 + f_{ion}^2 \omega^2 \right]} \tag{5.27}$$

$$k''_{ion}(\omega) = \frac{z_{cation} z_{anion} e^2 \left(1 - X_V(T,P)\right) N_{ion} f_{ion} \omega}{\varepsilon_0 M'_{red}(T,P) \left[\left(\omega_{ion}^2 - \omega^2 \right)^2 + f_{ion}^2 \omega^2 \right]} \tag{5.28}$$

$$M'_{red}(T,P) = \frac{m_{cation} \left(1 - X_V(T,P)\right) m_{anion}}{m_{cation} + \left(1 - X_V(T,P)\right) m_{anion}} \tag{5.29}$$

where the mole fraction of vacancies X_V is given by:

$$X_V(T,P) = \frac{[V_O^{\bullet\bullet}]}{[V_O^{\bullet\bullet}] + [O_O^{\times}]} = \frac{\left[\frac{1}{2}K_R^{\frac{1}{2}}(T)P^{-\frac{1}{4}} + \left(\frac{1}{2}A\right)^{\frac{3}{2}}\right]^{\frac{2}{3}}}{\left[\frac{1}{2}K_R^{\frac{1}{2}}(T)P^{-\frac{1}{4}} + \left(\frac{1}{2}A\right)^{\frac{3}{2}}\right]^{\frac{2}{3}} + [O_O^{\times}]}$$

$$\approx \frac{1}{[O_O^{\times}]}\left[\frac{1}{2}K_R^{\frac{1}{2}}(T)P^{-\frac{1}{4}} + \left(\frac{1}{2}A\right)^{\frac{3}{2}}\right]^{\frac{2}{3}} \qquad (5.30)$$

The constants f_{ion} and ω_{ion} may be determined by fitting Eqs. (5.24) and (5.25) or (5.27) and (5.28) for a known vacancy concentration — e.g., from doping — to plots of $k'_{ion}(\omega)/k''_{ion}(\omega)$ vs. ω data. The mole fraction of vacancies X_V [and, therefore, K_R, by way of Eq. (5.30)] may then be calculated from measurements of $k'_{ion}(\omega)$ and/or $k''_{ion}(\omega)$ for various temperatures and pressures.

The strength of this method lies in its simplicity. Its weakness lies in the relative complexity of the analysis required to extract the desired data.

2.5.2.3 From Micro-balance Measurements

We can also obtain the concentration of vacancies by way of a micro-balance. Vacancy concentration and as a result, the mass of a sample varies with oxygen partial pressure. Therefore a micro-balance may be used to record the weight change (and vacancy concentration) as a function of pressure. The vacancy concentration data can then be substituted into Eqs. (2.19), (3.1), or (3.29) to determine K_R. This method is perhaps the simplest way to determine K_R, although the accuracy may be insufficient.

2.6 Summary

We have significantly advanced the model on a theoretical basis. We have determined the most important parameters, u_e and K_R, for the model and identified several experimental methods to measure these parameters. In the next few months we will perform some of these experiments, determine the value of these parameters, use them to confirm the model, and then apply it to the bilayer to determine optimum relative thickness of the SDC and ESB layers.

REFERENCES

[1] O. Madelung, Introduction to Solid State Theory, (Springer-Verlag, Berlin Heidelberg 1978) chap. 8, pp 370.

[2] K. L. Duncan and E. D. Wachsman submitted to *Solid State Ionics*.

[3] O. Porat and H. L. Tuller, *J. Electroceramics* **1** (1997) 42.

[4] H. L. Tuller and A. S. Nowick, *ibid*. **126** (1979) 209.

[5] H. L. Tuller and A. S. Nowick, *ibid*. **122** (1975) 255.

[6] J. Hwang and T. O. Mason, *Zeitschrift fur Physikalische Chemie* **207** (1998) 21.

[7] K. Eguchi, T. Setoguchi, T. Inoue and H. Arai, *Solid State Ionics*, **52** (1992) 265.

[8] H. L. Tuller in: Nonstoichiometric Oxides, ed. O. Sorensen (Academic, New York, 1981) chap. 6, pp. 271.

[9] G. Brouwer, *Philips Res. Rep*. **9** (1954) 366.

[10] E. D. Wachsman and K. L. Duncan, Proceedings of the Sixth International Symposium on Solid Oxide Fuel Cell (SOFC VI) eds. S. C. Singhal and M. Doyika (The Electrochermical Society, 1999)

[11] B. A. Van Hassel, T. Kawada, N. Sakai, H. Yokokawa, M. Dokiya and H. J. M. Bouwmeester, *Solid State Ionics*, **66** (1993) 295.

[12] J. Newman, Electrochemical Systems, (Englewood Cliffs, N.J., Prentice-Hall, c1973) chap. 11.

[13] B. Steele, *Solid State Ionics*, **129** (2000) 95.

[14] M. Gödickemeier and L.Gauckler, *J. Electrochem. Soc.*, **145** (1998) 414

[15] M. Gödickemeier, K. Sasaki, L.Gauckler and I. Riess, *J. Electrochem. Soc.*, **144** (1997) 1635

[16] H. Inaba and H. Tagawa, *Solid State Ionics*, **83** (1996) 1.

NEUTRON DIFFRACTION STUDY OF OCCUPANCY AND POSITIONAL ORDER OF OXYGEN IONS IN PHASE STABILIZED CUBIC BISMUTH OXIDES

Sai Boyapati and Eric D. Wachsman
Department of Materials Science and Engineering
University of Florida
Gainesville, FL 32611

Bryan C. Chakoumakos
Neutron Scattering Section
Solid State Division
Oak Ridge National Laboratory
P. O. Box 2008, Bldg 7962
Oak Ridge, TN 37831-6393

The high temperature cubic bismuth oxide stabilized with Lanthanide dopants undergoes an order-disorder transition of the anion sublattice at about 600 °C. When annealed at temperatures below the transition temperature, oxygen ion conductivity undergoes a decay. Neutron diffraction studies have been performed to investigate the structural changes in the anion sublattice that result in the conductivity decay and the effect of dopant on the kinetics of decay. Atomic displacement parameters of oxygen ions were determined at low temperatures for the ordered and disordered structures to determine the static disorder in the oxygen sublattice of ordered and disordered structures.

INTRODUCTION

δ-Bi_2O_3, the high temperature cubic polymorph of bismuth oxide has the highest ionic conductivity among all the studied oxygen ion conductors [1]. This exceptional conductivity is due to the unique intrinsic defect fluorite structure of this material. The stoichiometry of the

material requires 25 percent of the oxygen sublattice to be vacant. Therefore, there is a random distribution of the oxygen ions over an excess number of equipotential sites, resulting in the mobility of all oxygen ions. The high temperature cubic phase undergoes a phase transformation to a poorly conducting monoclinic phase at 723°C. However, it can be stabilized by doping with several Lanthanide elements [2].

Due to their high ionic conductivity and the unique defect fluorite structure, there have been numerous studies on Lanthanide-doped bismuth oxides and these studies have been reviewed thoroughly [3,4]. Among the original structural models proposed for δ-Bi_2O_3were those of Sillen [5], Gattow [6] and Willis [7].

In the Gattow model, shown in Fig.1, each of the regular tetrahedral 8c sites has an equal probability of occupancy by oxygen ions. That is, the oxygen sites are all statistically occupied by 3/4 oxygen ion. This model implies that the oxygen sublattice is completely disordered with respect to occupancy of the 8c sites. This is consistent with the exceptionally high ionic conductivity, which is generally attributed to the defective nature of the oxygen sub-lattice. However, this model fails to explain the presence of a significant fraction of oxygen ions in the interstitial positions of the oxygen sublattice [8,9]. Therefore, this model of complete disorder does not accurately describe the structure.

In the Sillen model (Fig. 1), 3/4 of the regular tetrahedral sites in the lattice are occupied by oxygen ions and 1/4 of the sites are vacant with the oxygen vacancies ordered in the <111> directions. This model implies that the oxygen sublattice is ordered. However, in the x-ray and electron diffraction experiments of the high temperature structure, no long range <111> ordering of vacancies has been observed. An ordered structure is also inconsistent with the high ionic conductivity of the material above the order-disorder transition temperature.

In the Willis model (Fig. 1) the oxygen ions are displaced along four of the <111> directions from the regular tetrahedral sites towards the central octahedral vacant site. This gives occupancy of 3/16 at each of the 32 equivalent positions (32f sites) in the unit cell. This model describes the positional disorder in the oxygen sublattice. However, according to this model, there is no occupancy of oxygen ions in the regular tetrahedral sites, which is inconsistent with the neutron diffraction studies [8,9] of this material that show occupancy of oxygen ions in both 8c and 32f sites.

All three models are inconsistent with the observed experimental results and consequently, they need to be modified to explain the complex structural changes and their effect on the transport phenomena in the mobile sublattice and ultimately, the conductivity of the material. The neutron diffraction studies of Battle et al [8,9] and Verkerk et al [10,11] performed for the disordered anion sublattice show that the anion sublattice is a combination of the Gattow model (3/4 occupancy at 8c positions) and the Willis model (average occupancy of 32f positions). These studies are consistent with the high ionic conductivity of this material which is attributed to the disordered nature of the oxygen sublattice above the order-disorder transition temperature. Their studies did not indicate any type of <111> Sillen type of ordering in the disordered structures.

The phase-stabilized bismuth oxides undergo an order-disorder transition of the oxygen sublattice at about 600 °C resulting in a change in conductivity activation energy [10,11]. It has been reported by Wachsman et al that the conductivity of phase-stabilized bismuth oxides decays when annealed at temperatures less than the transition temperature. This degradation in conductivity with time was attributed to ordering of the mobile oxygen sublattice [12,13]. There has been some controversy regarding the theory of anion ordering and the aging phenomenon has been attributed to cation ordering by Fung et al [14]. The structural modeling of the oxygen

sublattice by Wachsman et al based on TEM and neutron diffraction has shown the decay in conductivity to be caused by the formation of a <111> alignment of oxygen vacancies as well as Willis type <111> displacements of oxygen ions [15,16]. The oxygen ion ordering mechanism was also confirmed by studying the dependence of kinetics of the aging phenomenon on dopant type and dopant concentration [17].

Neutron Diffraction studies were performed to investigate the effect of dopant on the structural changes in the oxygen sublattice resulting in the conductivity decay. The oxygen sublattice of both the ordered and the disordered structures of bismuth oxide doped with Yb, Er, Y, Ho, and Dy were studied. The change in occupancy of oxygen ions in the 8c and 32f positions was determined for each dopant. For the samples doped with Yb, we calculated the positional disorder in the ordered and the disordered structures by measuring the mean isotropic atomic displacement parameters of oxygen ions at low temperatures.

EXPERIMENTAL

Polycrystalline samples of M_2O_3-Bi_2O_3 (M = Yb, Er, Y, Ho, Dy) were prepared by a solid state reaction from a stoichiometric mixture of Bi_2O_3 (99.999% pure) and M_2O_3 (99.99% pure) powders. The powders of required composition (25% M_2O_3) were mixed and ground. The mixed powders were calcined at 800 °C for 16 hours, and then ground again and pressed into pellets of 2.5 cm diameter, which were subsequently sintered in air at 900 °C for 16 hours. Some of the pellets were then aged in air at 500 °C for 300 hours.

The neutron diffraction studies were performed at the High Flux Isotope Reactor (HFIR) facility at Oak Ridge National Laboratory. For our studies, we used the high-resolution neutron powder diffractometer. The monochromator is a (115) Ge crystal, which can be oriented to select incident wavelengths of 1.0, 1.4, 2.2, and 4.2Å. An array of 32 equally spaced (2.7deg.) Helium

detectors, each with a 6' mylar foil Soller collimator, can be step-scanned over a range of up to 40deg. for scattering angles between 11 deg. and 135deg. Soller slit collimators of 12' and 20' are positioned before and after the monochromator crystal, respectively.

Powdered samples were held in 1 cm dia vanadium cans with ceramic lids. The data was collected at room temperature for the aged and the unaged samples of M_2O_3-Bi_2O_3 (M = Yb, Er, Y, Ho, Dy). The data was also collected for Yb_2O_3-Bi_2O_3 at 11 K, 75 K, 150K, and 225K by placing the powdered sample in a Helium refrigerator. The structural parameters were refined using the software General Structural and Analysis System (GSAS) developed by Allen C. Larson and Robert B. Von Dreele at Manuel Lujan, Jr. Neutron Scattering Center, Los Alamos National Laboratory [19].

RESULTS AND DISCUSSION

The neutron diffraction data was refined using the least squares Rietveld refinement procedure using the software GSAS. During the refinement process, the fraction of oxygen ions at three different sites (8c, 32f, and 48i) were used as variables. In addition, the x values of 32f (x,x,x) and 48i (0.5,x,x) sites were also allowed to vary. As a starting point, we refined the diffraction data of both aged and unaged samples with all the dopants assuming Sillen, Gattow, and Willis models. The residuals ($\chi 2$) for these models are shown in Table 1 for each of the samples.

Table 1(a). Residuals ($\chi 2$) for Rietveld Refinement based on Sillen Model

Dopant	Disordered Structure	Ordered Structure
Yb	179	75
Er	171	86
Y	183	82
Ho	190	84

Dy	166	96

Table 1(b). Residuals (χ2) for Rietveld Refinement based on Gattow Model

Dopant	Disordered Structure	Ordered Structure
Yb	128	180
Er	142	192
Y	156	183
Ho	133	186
Dy	122	193

Table 1(c). Residuals (χ2) for Rietveld Refinement based on Willis Model

Dopant	Disordered Structure	Ordered Structure
Yb	135	24
Er	152	19
Y	140	20
Ho	161	44
Dy	122	70

From the Tables, it is clear that none of the models by themselves is consistent with the observed results for either the ordered or the disordered cases. The residuals are very high for the Gattow model both for ordered and disordered data sets. They are relatively low with the Sillen model with the ordered data set. In general, it can be noted that while a good fit is not obtained for either of these models by themselves, the Sillen model is a better fit for the ordered structure and the Gatow model is a better fit for the disordered structure. In addition, it can be noted that the deviations are significantly lower in the case of the Willis model for ordered structures. This indicates the importance of displacements during the ordering process. The residuals obtained however, are still large enough to merit further refinement by modifying the above models. The

refinements were carried out till the residuals approached zero indicating a good fit with the raw data, and consequently, the validity of the structural model.

The TEM diffraction patterns of the ordered structures give additional weak reflections which correspond to an ordered structure consisting of <111> vacancy ordering [13,15,16]. Therefore, we must take the occupancy of regular 8c sites ("occupancy ordering"), corresponding to the Sillen model into consideration for the ordered structures. The previous neutron diffraction study on $(Bi_2O_3)_{0.80}(Er_2O_3)_{0.20}$ has shown that there is an extensive displacement of oxygen ions from the regular 8c positions to the 32f interstitial positions ("positional ordering") corresponding to the Willis model [20]. This study also indicates that the fraction of oxygen ions in the 48i sites does not change significantly with aging. Therefore, we must take into consideration the combination of Sillen (occupancy ordering) and Willis (positional ordering) models for the ordered structures.

In the case of disordered structures, there have been neutron diffraction studies [5,6] which show no occupancy ordering. However, these studies also show that there is a significant fraction of oxygen ions in the 32f positions (positional ordering). Therefore, for the refinement of disordered structures, we start with a combination of random occupancy and positional ordering, i.e, the combination of Gattow and Willis models respectively.

The oxygen ions are distributed among three sites- 8c, 32f and 48i in the fluorite unit cell. Ideally, we should vary the fractions of oxygen ions in all three sites simultaneosly. However, this leads to either a divergence of equations, or a convergence with high residuals and the total sum of oxygen ions greater than 6. In order to achieve stable convergence, we had to constrain the fraction of oxygen ions in one of the sites to be constant and vary the other pair. Since the fraction of oxygen ions in 48i sites does not vary significantly with aging, we fixed the 48i site

occupancy at 0.3. The isotropic atomic displacement parameters were also assumed to be constant for each case

The residual values of refinement are plotted against the occupancy of oxygen ions in 8c positions for both ordered and disordered structures. The results are shown in Figures 2, 3, 4, 5 and 6 for Yb, Er, Y, Ho, and Dy respectively. From the figures, we can see that the fraction of oxygen ions displaced from the 8c sites during the ordering process is least for Dy doped structure and highest for Yb and Er doped structures. The final values with minimum residuals after refinement (less than 1) are shown for all the dopants in Table 2. The time constants for conductivity decay (aging), taken from [17] and the change in structural parameters of oxygen sublattice due to aging, 1- 8c(aged)/8c(unaged) are also shown in the Table for each dopant.

The change in oxygen ion occupancy due to doping is plotted as a function of time constant for aging in Figure 7. From the figure, it is clear that the higher the kinetics of conductivity decay, the higher is the displacement of oxygen ions from the tetrahedral 8c sites to the interstitial 32f positions. This clearly demonstrates the correlation between the structural arrangement of the oxygen sublattice and the decay in ionic conductivity. This also confirms the anion ordering theory to describe the aging process.

Table 2. Structural Parameters of Aged and Unaged Structures *

Dopant	Time Constant for Aging (h)	0ccupancy in 8c sites		Occupancy in 32f sites		Change in occupancy due to aging
		Unaged	Aged	Unaged	Aged	1- 8c(aged)/8c(unaged)
Yb	4.177	1.08	0.06	1.62	2.64	0.9444
Er	24.823	1.16	0.08	1.54	2.62	0.9310
Y	53.789	1.17	0.10	1.53	2.60	0.9145
Ho	79.412	1.26	0.37	1.44	2.33	0.7063

Dy	170.00	1.32	1.14	1.38	1.56	0.1363

*The remaining fraction (0.3) of oxygens in the anion sublattice occupy the 48 i sites

The occupancy and positional order of the anion sublattice obviously affect the oxygen ion transport mechanism. This mechanism therefore needs to include the occupancy of interstitial positions. These points are discussed in detail in [18].

Static Disorder in Yb_2O_3-Bi_2O_3

The atomic displacement parameters have to be taken into account during the Rietveld refinement of crystal structures because they affect the nature of the diffraction patterns. The atomic displacements arise due to thermal and static disorder. At room temperature, the displacements due to the thermal disorder are significantly higher. Therefore, in the room temperature experiments, these displacements are taken into consideration and are usually reported as sources of error in the refinement process.

The displacement parameters were allowed to vary during the refinement of data taken at low temperatures for Yb_2O_3-Bi_2O_3 . The isotropic atomic displacements are plotted as a function of temperature in Figure 8. From the Figure, we can see that the displacement amplitudes for the ordered structure are lower than those of the disordered structure at all temperatures. In both cases, the displacement parameters increase linearly with temperature. Extrapolating the approximate straight lines to zero, we can see that the static or structural contribution to the atomic vibration at 0 K is significantly higher for the disordered structure.

From Figure 8, we can also see that the slope corresponding to the disordered structure is higher than that of the ordered structure. This indicates that the thermal contribution to the vibration of oxygen ions is higher for the disordered structure. Differential thermal analysis (DTA) of erbia stabilized bismuth oxide shows a change in slope at the order-disorder transition temperature (about 600 °C) [12]. That study shows that the slope is 4.7 x 10^{-5} °C/mg/°C below

the transition temperature and 7.6 x 10^{-5} °C/mg/°C above the transition temperature. Since these slopes are proportional to heat capacity, the increase in slope is attributed to a greater degree of vibrational freedom in the disordered state. This is consistent with the slopes of the lines shown in Figure 8. The slope of the line for the ordered structure is 8.53 x 10^{-5} Å^2/K and the slope for the disordered structure is 16.36 x 10^{-5} Å^2/K. This is clearly consistent with the previous DTA study and shows that due to higher degrees of freedom for oxygen ions in the disordered structure, the thermal contribution to atomic vibrations is significantly higher. Moreover, the ratio of the DTA slope above the transition temperature to that below the transition temperature is 1.62 and the corresponding ratio of the slopes of the displacement lines is 1.92. These two independent measurements show a consistent increase in the thermal disorder of the structure above the transition temperature compared to that of the ordered structure below the transition temperature.

CONCLUSIONS

The decay in oxygen ion conductivity in cubic bismuth oxides stabilized by isovalent Lanthanide cations when annealed below the order-disorder transition temperature is due to ordering of the oxygen sublattice. The <111> vacancy ordering is accompanied by the displacement of oxygen ions from the regular tetrahedral 8c sites to the interstitial 32f sites. As a result, the ordered structures cannot be described on the basis of any single existing structural models for this material. The refinements of neutron diffraction data show that the disordered structures can be satisfactorily described in terms of a combination of Gattow and Willis models, whereas the ordered structures are consistent with a mixed Sillen - Willis models. The low temperature neutron diffraction data of ordered and disordered structures of Yb_2O_3-Bi_2O_3 show that both static and thermal disorder of oxygen ions in the disordered structures is higher than that in the ordered structures.

ACKNOWLEDGEMENT

We would like to thank the US Department of Energy (Contract # DE-AC26-99FT40712) for supporting this work.

REFERENCES

1. T. Takahashi, H. Iwahara and Y. Nagai, *J. Appl. Electrochem.*, **2** 97 (1972)

2. T. Takahashi, and H. Iwahara, *Mater. Res. Bull.*, **13** 1447 (1978)

3. A. M. Azad, S. Larose, and S. A. Akbar, J. Mat. Sci., **29** 4135 (1994)

4. P. Shuk, H. D. Wiemhofer, U. Guth, W. Gopel, and M. Greenblatt, *Solid State Ionics*, **89** 179 (1996)

5. L. G. Sillen, *Ark. Kemi. Mineral. Geol*. **12A** 1 (1937).

6. V. G. Gattow and H. Schroder, *Z. Anorg. Allg. Chem.*, **318** 197 (1962).

7. B. T. M. Willis, *Acta Crystallogr*. **18** 75 (1965).

8. P. D. Battle, C. R. A. Catlow, J. W. Heap, and L. M. Moroney, *J. Solid State Chem.*, **63** 8 (1986)

9. P. D. Battle, C. R. A. Catlow, J. W. Heap, and L. M. Moroney, *J. Solid State Chem.*, **67** 42 (1987)

10. M. J. Verkerk, A. J. Burggraaf, *Solid State Ionics*, **3/4** 463 (1981)

11. M. J. Verkerk, G. M. H. Van De Velde, A. J. Burggraaf, and R. B. Helmholdt, *J. Phys. Chem. Solids*, **43** 1129 (1982)

12. E. D. Wachsman, N. Jiang, D. M. Mason, and D. A. Stevenson, *Proc. Electrochem. Soc.*, **89-11** 15 (1989)

13. N Jiang, R. M. Buchanan, F. E. G. Henn, A. F. Marshall, D. A. Stevenson, and E. D. Wachsman, *Mater. Res. Bull.*, **29**, 247 (1994)

14. K. Z. Fung, J. Chen, and A. V. Virkar, *J. Am. Ceram. Soc.,* **76**, 2403 (1993)

15. E. D. Wachsman, S. Boyapati, M. J. Kaufman, and N. Jiang, *Solid State Ionic Devices : Proc. Electrochem.* Soc., **42** (1999)

16. E. D. Wachsman, S.Boyapati, M. J. Kaufman, and N. Jiang, Accepted for publication, *J. Amer. Cer. Soc.*

17. N. Jiang and E. D. Wachsman, *J. Am. Ceram. Soc*., **82**, 3057 (1999)

18. S. Boyapati, E. D. Wachsman, and N. Jiang, Submitted to *Solid State Ionics*

19. A. C. Larson and R. B. Von Dreele, *GSAS, General Structural and Analysis System,* Report LAUR-86-748. Los Alamos National Laboratory, Los Alamos, NM

20. N. Jiang, R. M. Buchanan, D. A. Stevenson, W. D. Nix, Li Ji-Zhou, and Yang Ji-Lian, *Materials Letters* **22**, 215 (1995)

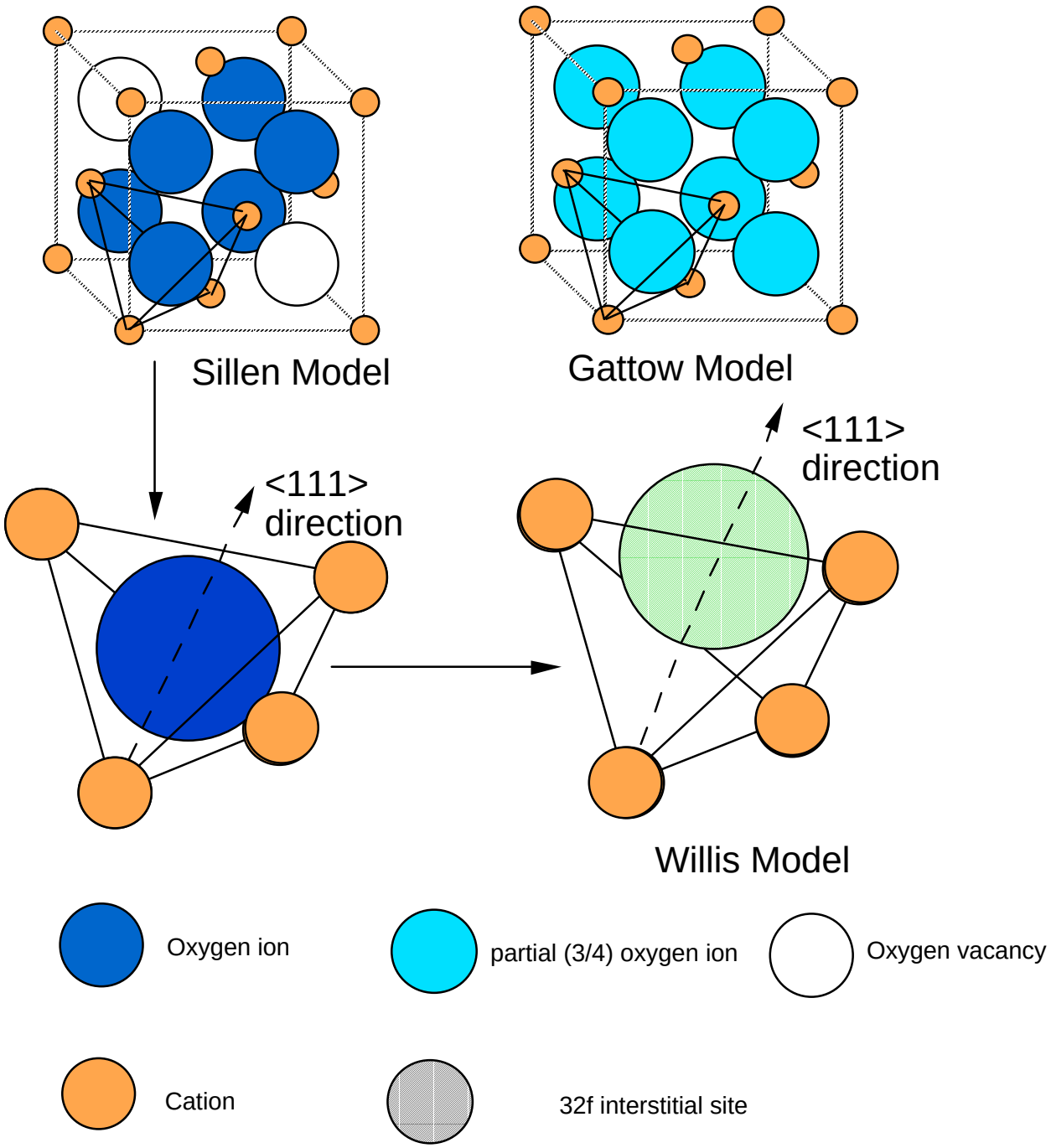

Figure 1. Structural models for cubic bismuth oxide

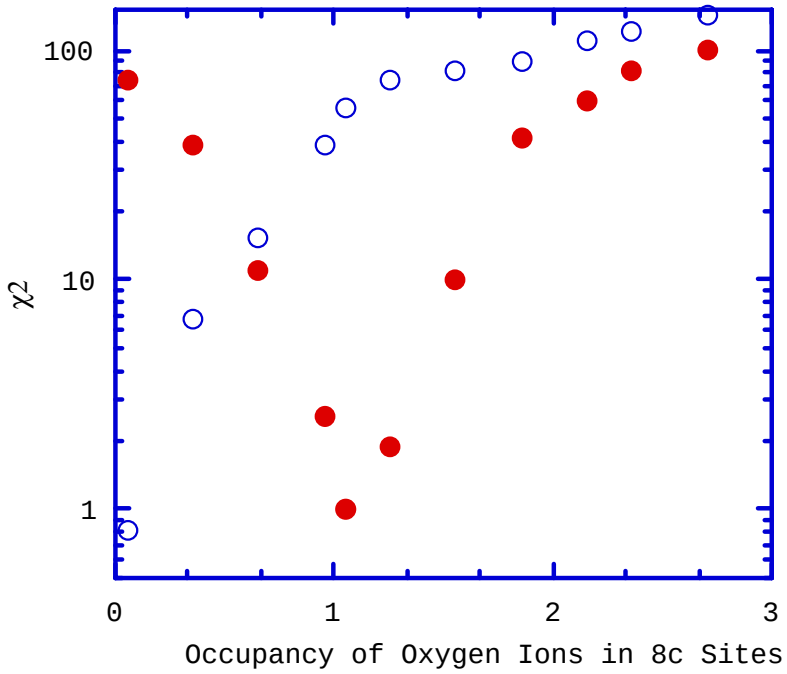

Fig. 2 Residuals of refinement as a function of oxygen ion occupancy for 25 YbSB for ordered structures (open circles) and disordered structures (filled circles)

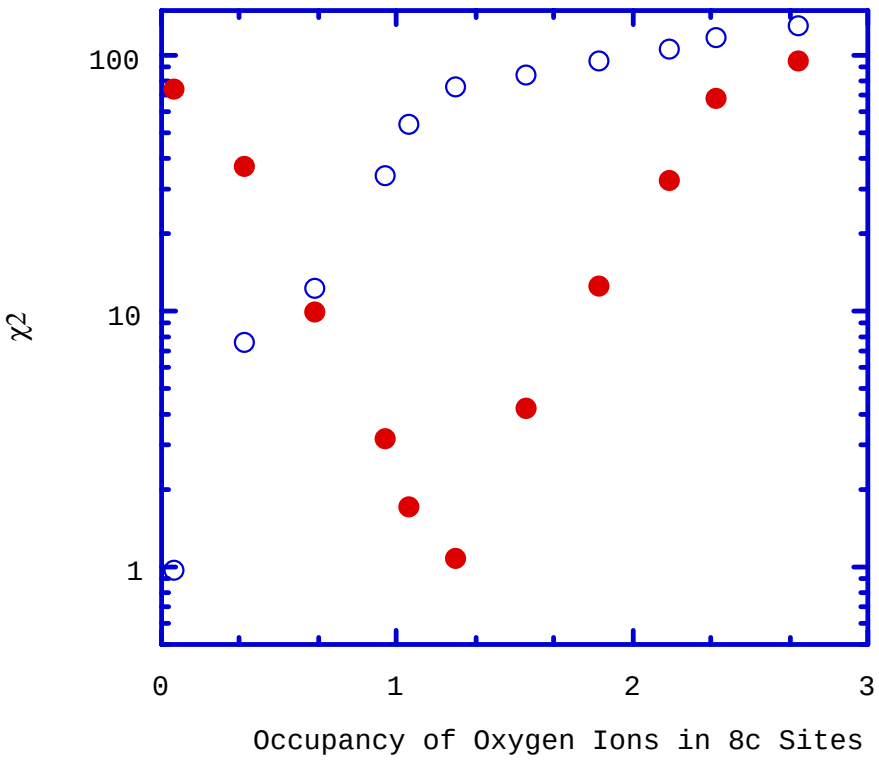

Fig. 3 Residuals of refinement as a function of oxygen ion occupancy for 25 ErSB for ordered structures (open circles) and disordered structures (filled circles)

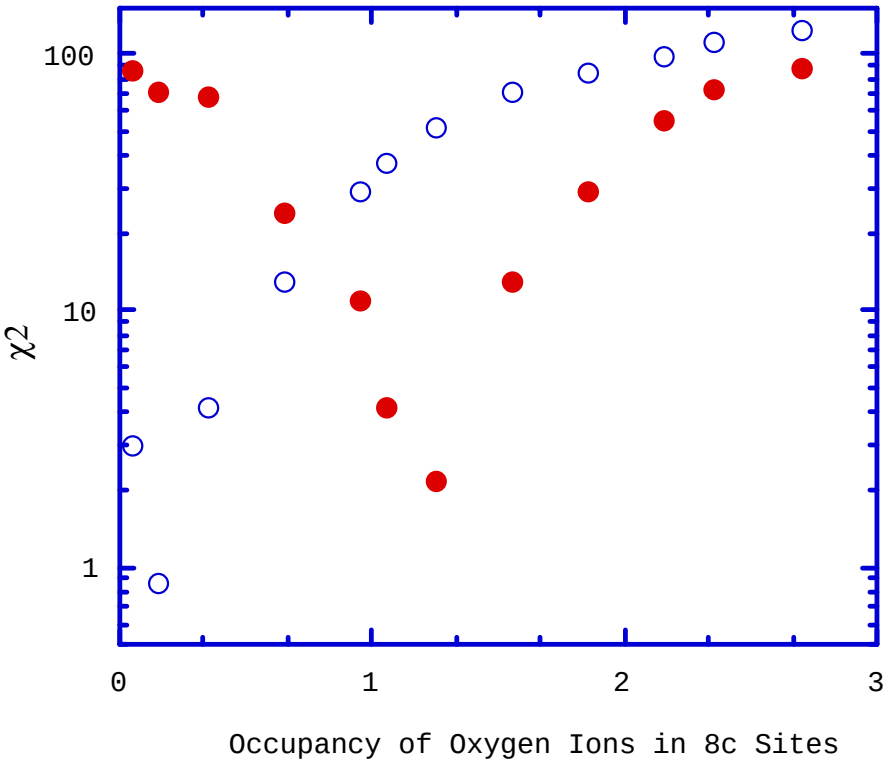

Fig. 4 Residuals of refinement as a function of oxygen ion occupancy for 25 YSB for ordered structures (open circles) and disordered structures (filled circles)

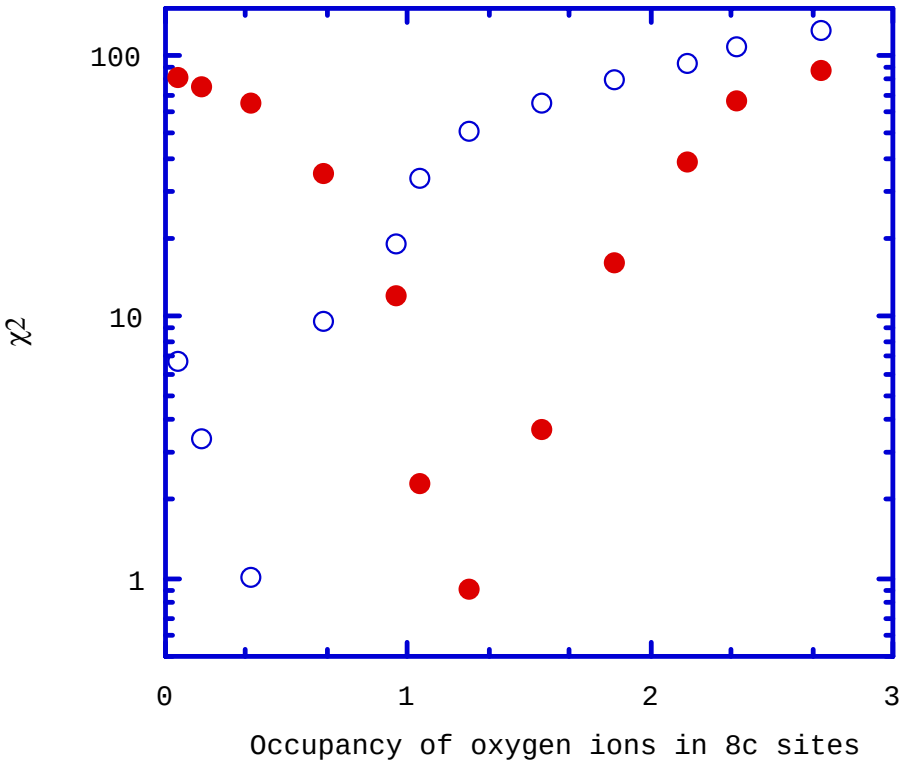

Fig. 5 Residuals of refinement as a function of oxygen ion occupancy for 25 HoSB for ordered structures (open circles) and disordered structures (filled circles)

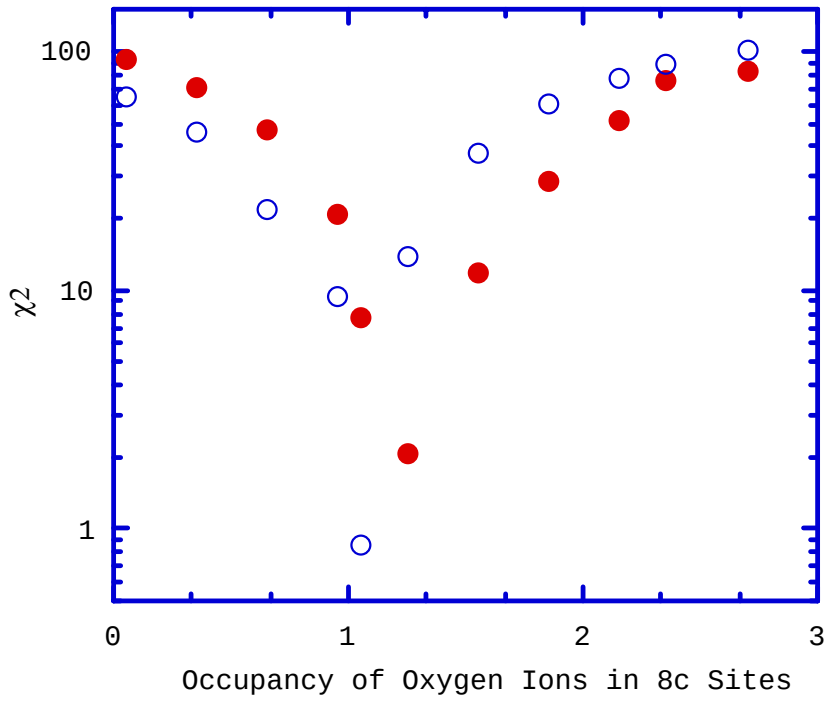

Fig. 6 Residuals of refinement as a function of oxygen ion occupancy for 25 DySB for ordered structures (open circles) and disordered structures (filled circles)

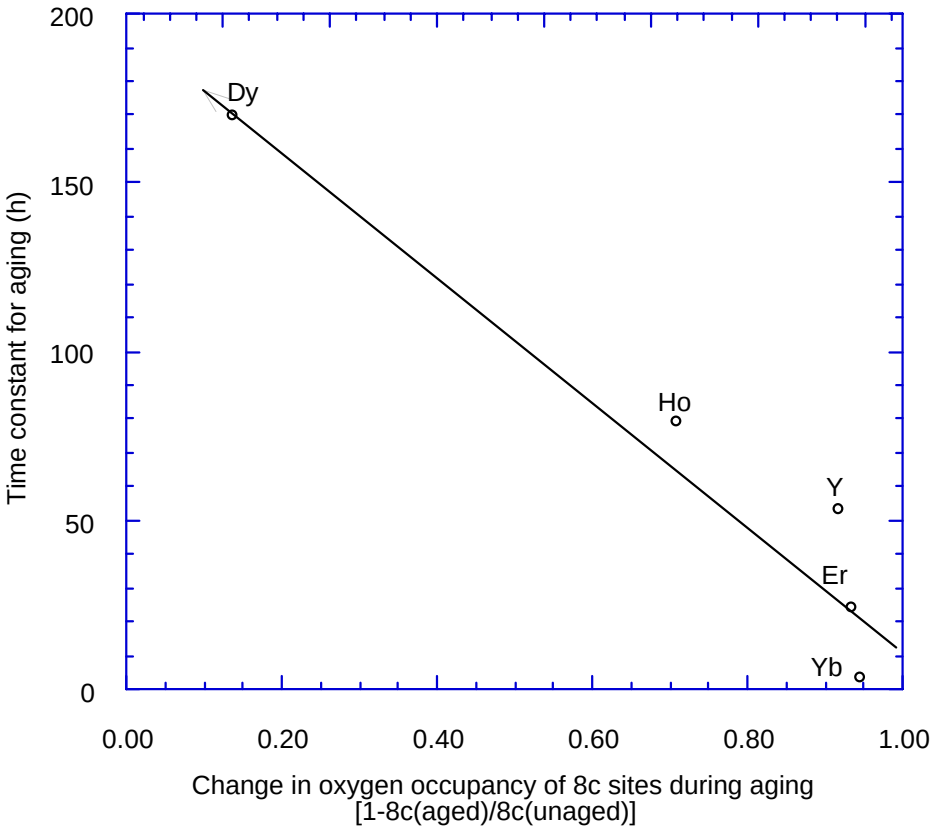

Figure 7 Correlation between time constant for aging and change in oxygen ion occupancies

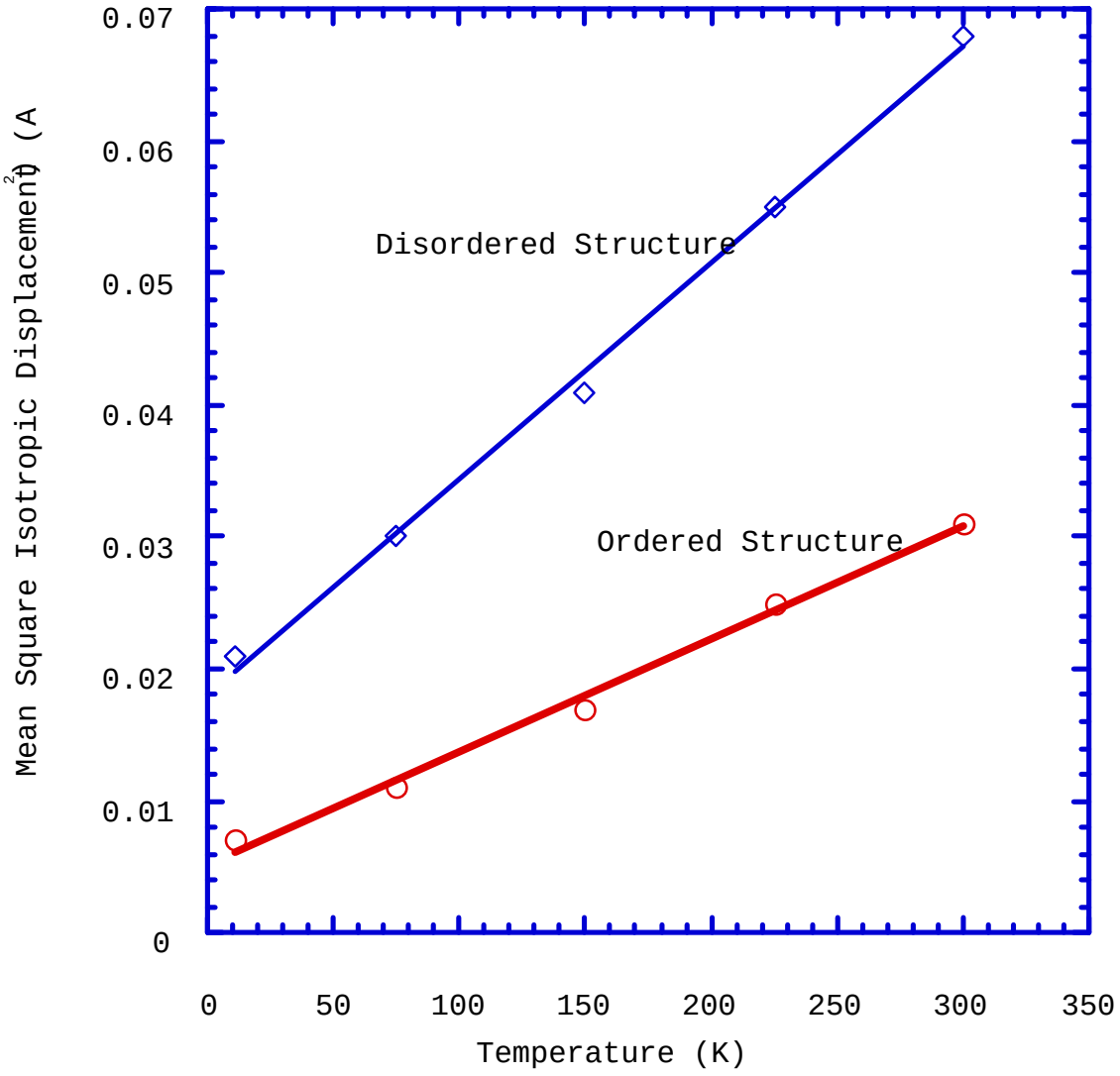

Figure 8. Displacement parameters of oxygen ions as a function of temperature for Yb_2O_3 - Bi_2O_3

Effect of Oxygen Sublattice Ordering on Interstitial Transport Mechanism and Conductivity Activation Energies in Phase-Stabilized Cubic Bismuth Oxides

Sai Boyapati, and Eric D. Wachsman
Department of Materials Science and Engineering
University of Florida
Gainesville, FL 32611

Naixiong Jiang
Materials Research Center
SRI International
Menlo Park, CA 94025

Bismuth oxide doped with isovalent rare earth cations retains the high temperature defective fluorite structure upon cooling down to room temperature. However, these doped materials undergo an order-disorder transition of the oxygen sublattice at about 600 °C. When annealed at temperatures less than the transition temperature the oxygen sublattice continues to order, and consequently oxygen ion conductivity undergoes a decay. However, the conductivity activation energies of the ordered structures after extended aging at 500 °C were observed to be lower than those of the structures prior to aging. Modeling of ordered structures based on TEM diffraction patterns indicates a <111> vacancy ordering in the anion sublattice. Neutron diffraction studies show additional structural changes in the oxygen sublattice due to ordering. These studies indicate that the ionic conductivity is dependent on the distribution of oxygen ions between the regular 8c sites and the interstitial 32f sites in the fluorite structure. Based on the TEM and neutron diffraction studies and conductivity activation energies of the ordered and disordered structures, an interstitial transport mechanism for oxygen ions is proposed.

Keywords : Oxygen ion conductors, Bismuth oxide, Ionic transport, Polarizability, Conductivity pre-exponential, Fluorite structure

PACS Codes: 66.30.Dn, 61.43.Bn, 84.60.Dn, 61.72.Bb

INTRODUCTION

δ-Bi_2O_3 has a defect fluorite structure in which 25 percent of the sites in the oxygen sub-lattice are vacant. The high intrinsic defect concentration gives high ionic conductivity to this material. Pure bismuth oxide transforms to monoclinic α-phase on cooling below 730 °C. The phase transformation leads to a discontinuous drop in conductivity. The high temperature phase can be stabilized to room temperature by the addition of several Lanthanide dopants [1-2]. However, in the phase-stabilized bismuth oxides, an order-disorder transition of the oxygen sublattice occurs at around 600 °C resulting in a change in conductivity activation energy at the transition temperature [3]. Below the order-disorder transition temperature, the oxygen sublattice continues to order with time, leading to a decay in ionic conductivity [4-8].

Disordered Structure Above the Transition Temperature

The unit cell of cubic bismuth oxide consists of four cations occupying the FCC positions and six anions occupying the eight tetrahedral positions. The nature of the arrangement of the six anions and the two anion vacancies has been a subject of controversy. Several contrasting models have been proposed to describe the high temperature (above 600 °C) disordered anion sublattice.

In the Gattow model [9], each of the regular tetrahedral 8c sites has an equal probability of occupancy by oxygen ions. That is, the oxygen sites are all statistically occupied by 3/4 oxygen ion. This model implies that the oxygen sublattice is completely disordered with respect to occupancy of the 8c sites. This is however inconsistent with the neutron diffraction studies of Battle et al [10,11] which show occupancy of oxygen ions in 32f interstitial sites and also possible short range ordering of the anion sublattice. In the Sillen model [12] 3/4 of the regular tetrahedral sites in the lattice are occupied by oxygen ions and 1/4 of the sites are vacant with the

oxygen vacancies ordered in the <111> directions. This model implies that the oxygen sublattice is fully ordered which is inconsistent with the high ionic conductivity of the material. In the Willis model [13], the oxygen ions are displaced along four of the <111> directions from the regular tetrahedral sites towards the central octahedral vacant site. This gives occupancy of 3/16 at each of the 32 equivalent positions (32f sites) in the unit cell. None of these models by itself is consistent with the experimental neutron diffraction results as discussed in our previous work [14]. However, a combination of Gattow and Willis models is consistent with the experimental results of the high temperature disordered structure.

Effect of Structure on Conductivity Mechanisms in the Disordered Structure

Based on the structural models discussed above, several theoretical and experimental studies have been performed to study disordered fluorite structures in general, δ-Bi_2O_3 in particular, and the effect of structure on conductivity.

Koto *et al* studied the structure of β-PbF_2 and the transport mechanism of the mobile ions through the rigid cation sublattice [15]. They calculated the most favorable conduction pathway by using the interaction energies of the mobile ions in the ionic solid. Their results can be summarized as follows.

- The minimum energy path for the mobile ions through the static cation sublattice involves motion from one tetrahedral site to the next by following a path that passes close to, but not through the center of the intermediate octahedral site.
- The potential energy calculations based on this minimum energy path indicate the presence of eight metastable positions near, but slightly displaced from the centers of the octahedral sites.

(The off-center displacements predicted by this model almost match with the interstitial positions determined by neutron diffraction [10,11,14].)

- For all studied cases, the energy profile along a direct tetrahedral-tetrahedral path was found to produce a considerably greater activation enthalpy than for the tetrahedral-octahedral-tetrahedral path. This observation is rationalized by the fact that the barrier for migration for a direct <100> jump between two tetrahedral sites is higher due to the rigid cation lattice.

Neutron diffraction studies of cubic bismuth oxides by Battle *et al* [10, 11] and us [14] show that a significant fraction of oxygen ions occupy the 32f interstitial positions. These positions are located on the minimum energy conduction pathway calculated by Koto et al [15]. Therefore, their conduction model calculated for lead fluoride can be applied to the fluorite structure of δ-Bi_2O_3. From these studies, it can be concluded that the interstitial 32f positions are located immediately adjacent to the transition state or saddle point for the transport of oxygen ions between the regular tetrahedral sites.

Jacobs *et al* carried out extensive computational studies to determine the nature of the defect structure of δ-Bi_2O_3 [16-18]. Their computational studies can be summarized as follows

- The <111> vacancy superlattice is metastable. That is, it is energetically unfavorable for long range ordering of anion vacancies in the <111> directions. Therefore, they show that it is energetically favorable for the formation of <110> defects in the <111> arrangement.
- The <110> defects that form in <111> lattice are limited in their concentration due to their electrostatic interactions.

- The oxygen ions are displaced slightly towards the central octahedral void during their transport between tetrahedral sites. These displacements are not as extensive as those observed by Battle *et al* or those predicted by Koto *et al*.

The neutron diffraction studies of Battle *et al* reveal the presence of extensive short range ordering of oxygen ions [10,11]. They observed that the extent of short range ordering increases with increasing dopant concentration. They propose that pure bismuth oxide has a tendency to form a <110> vacancy structure rather than a <111> structure because of the high polarizability of the bismuth ion, due its stereochemically active lone-pair of electrons. The <110> vacancy arrangement clearly facilitates a greater degree of disorder in the anion sublattice. The dopant rare earth oxides have lower polarizability than bismuth and therefore prefer the <111> vacancy structure. Therefore, in doped bismuth oxides the oxygen vacancies have a greater tendency to align along <111> directions.

Based on the experimental and theoretical calculations, we conclude that the high temperature fluorite structure of bismuth oxide consists of a disordered oxygen sublattice, which has a short range ordering of oxygen vacancies along <111> directions. The tendency for this type of ordering increases with increasing dopant concentration. In addition, the displacement of oxygen ions from the regular 8c sites to the interstitial 32f sites plays a significant role in the conductivity mechanism of bismuth oxide. From our previous neutron diffraction work [16], we have shown that the displacement of oxygen ions occurs simultaneously with vacancy ordering. Thus, it appears there are two types of ordering phenomenon in the defect fluorite structure of stabilized cubic Bi_2O_3. The ordering of vacancies along <111> directions and the displacement of oxygen ions from the regular to the interstitial sites.

From the above studies, it is clear that the transport mechanism in cubic disordered bismuth oxides involves the occupancy of interstitial sites, and the fraction of oxygen ions occupying these sites affects the conductivity of the material. The interstitial transport path (proposed by Koto *et al*) is indicated in Figure 1 both for Sillen and Gattow occupancy of 8c sites. The Figure illustrates the most energetically favorable path for <100> transport of an oxygen ion from the regular tetrahedral position 8c, through an interstitial 32f position, towards the central octahedral site (but not through it), through another 32f position, to a vacant tetrahedral site (8c) adjacent to the original tetrahedral site.

Obviously, this path has a higher jump distance than a direct <100> jump between the regular tetrahedral sites. However, it is preferred because of the lower energy barrier due to the vacant octahedral site. It should be noted that the only stable occupancy of the oxygen ions along this path is found at 32f positions [5,6]. Consequently, the occupancy of oxygen ions in these sites is important in the conduction mechanism.

Ordered Structure Below the Transition Temperature

It has been observed that the conductivity of phase-stabilized bismuth oxides undergoes a decay in conductivity when annealed below 600 °C [4-8]. This decay, termed as aging occurs due to the time and temperature dependent ordering of oxygen ions below the order-disorder transition temperature. Transformation to the ordered structure could not be detected by XRD because of weak scattering of x-rays by oxygen ions. It is however observed by TEM diffraction which show the formation of a superlattice [19,20]. The kinetics of the ordering phenomenon depend upon the ionic radius of the dopant cation. Among the studied compositions, it has been

shown that the rate of aging is least for Dy^{3+} ion and highest for Yb^{3+} ion [7]. Several structural models for the ordered structures have been studied by us, and we have shown that a <111> vacancy ordering is most consistent with the TEM diffraction studies [8,19]. The aging phenomenon has also been studied by Fung et al who propose a dopant cation ordering mechanism to explain the decay in oxygen ion conductivity [20]. Neutron diffraction experiments indicate that the vacancy ordering process is accompanied by the displacement of nearly all the oxygen ions from the 8c to 32f positions [6,14]. These displacements were taken into account in the modeling of the ordered structures [8,19]. It has been discussed in the analysis of neutron diffraction results that a combination of Sillen and Willis models is consistent with the ordered structure [14].

From the above discussion, it is clear that the structure of both the ordered (below 600 °C) and the disordered (above 600 °C) structures is quite complex and has been a subject of controversy. In order to understand the ionic conductivity of the material, it is imperative to elucidate the effect of structure on conductivity and conductivity activation energy.

In this work, we studied the structure of both ordered and disordered samples of bismuth oxide stabilized with several dopants (Yb, Er, Y, Ho, and Dy). We also determined the conductivity activation energies of each composition both prior to and after aging. Based on these results, we describe a model for an interstitial transport mechanism, whereby oxygen ions move from a filled to an adjacent empty anion site by migration through intermediate interstitial sites. Using the structural information of the compositions, we calculated the conductivity pre-exponentials and compared the values with the observed values to demonstrate the validity of the mechanism.

EXPERIMENTAL

Polycrystalline samples of M_2O_3-Bi_2O_3 (M = Yb, Er, Y, Ho, Dy) were prepared by a solid state reaction from a stoichiometric mixture of Bi_2O_3 (99.999% pure) and M_2O_3 (99.99% pure) powders. The powders of required composition were mixed and ground. The mixed powders were calcined at 800 °C for 16 hours, and then ground again and pressed into pellets of 2.5 cm diameter, which were subsequently sintered in air at 900 °C for 16 hours.

The as-sintered pellets were polished to obtain planar surfaces. Engelhard gold paste was applied to the polished surfaces and annealed at 800 °C for 4 hours to obtain porous gold electrodes. A one inch long gold wire was attached to each gold electrode using the gold paste, and annealed at 800 °C for 4 hours. Some of the pellets were then aged in air at 500 °C for 300 hours. Conductivity measurements over a frequency range 20 Hz to 1 MHz were made using a two-probe AC impedance method with an HP 4282A precision impedance LCR (inductance-capacitance-resistance) meter.

Conductivity activation energies were determined from plots of σT vs. 1/T below the order-disorder transition temperature. For the disordered structures the samples were quenched below the order-disorder transition temperature for measurement of conductivity, with minimal effect of aging, then heated above the transition temperature to disorder the anion lattice and then quenched again to the next temperature. The aged samples were cooled down rapidly from 500 °C after 300 hours and the activation energies were determined from the Arrhenius plots in the temperature range 200 - 400°C where the rate of aging is relatively low. From these experiments,

we could compare the activation energies of aged and unaged samples under similar temperature ranges without any significant time dependence to the data. The neutron diffraction studies were performed at the High Flux Isotope Reactor (HFIR) facility at Oak Ridge National Laboratory as described in [14].

RESULTS AND DISCUSSION

I. Neutron Diffraction Results

Aging results in the formation of a long range <111> vacancy superlattice (described in 19) and the displacement of oxygen ions from 8c to 32f sites. The analysis of neutron diffraction results and the refinement process are described in [14]. The changes in structural parameters of anion sublattice after 300 hours of aging are shown in Table 1 for several dopants. Time constants for the exponential decay in conductivity (aging), taken from our previous work [7] are also shown in Table 1.

From the Table, it is clear that the fraction of oxygen ions in interstitial 32f positions is higher than that in the regular 8c sites for both aged and unaged samples. In addition, the fraction of oxygen ions occupying the 32f positions increases significantly with aging. Therefore, this type of preferential occupancy of oxygen ions in the interstitial 32f positions is part of the aging process. The higher the occupancy of oxygen ions in the regular 8c sites, and lower the occupancy of oxygen ions in the intermediate 32f positions (both before and after aging), the higher the time constant for aging.

The oxygen ions in 32f positions are therefore least stable in Dy doped sample and most stable in Er and Yb doped samples. This could be due to the lower polarizability of the dopant

cation, which depends upon its ionic radius and electronic configuration. However, it is not clear whether all the rare earth dopants follow this generalized assumption. From our results, it is clear that Dysprosium ions do not cause extensive oxygen ion displacements or <111> vacancy ordering even after 300 hours of aging.

II. Effect of Dopant Polarizability on Kinetics of Aging

Shirao *et al*[22] studied the correlation between the polarizability and the effective ionic radius in lanthanide elements. They arrived at an empirical relationship indicating that the polarizability is proportional to the cube of ionic radius. Using their relationship, we calculated the polarizabilities of the dopant cations. The correlation between the polarizability of dopant cations and time constant for aging is shown in Figure 2. From the figure, it is clear that there is a strong linear dependence between the dopant cation polarizability and the kinetics of aging. This is also consistent with the fact that the conductivity in cubic bismuth oxides is reduced due to substitution of highly polarizable bismuth ions with less polarizable lanthanide ions in the cation sublattice. In their structural analysis, Battle et al propose that bismuth ions are highly polarizable due to the presence of lone-pair of electrons in their outer shell [10,11]. This high polarizability makes it very unlikely for a <111> vacancy arrangement in the oxygen sublattice. They also proposed that a less polarizable ion such as Y^{3+} would prefer a <111> vacancy arrangement. Our results are therefore clearly consistent with this analysis.

Since there is a relationship between the polarizability and the kinetics of aging, there should also be a relationship with the dielectric constant. Therefore, the dielectric constants were calculated from the bulk components of the AC impedance spectra for unaged samples at 200°, 250°, and 300°C. As shown in Figure 3 there is a linear relationship between the log of the time

constant and the log of the dielectric constant for all of the dopants except Yttrium. This linear relationship confirms the effect of polarizability of cation sublattice on kinetics of ordering of the oxygen sublattice. The fact that Y does not belong to the same periodic group as the rest of the dopants may explain its deviation from the linear dependence observed with the lanthanide dopants. The polarizability depends upon the shielding of nucleus by the valence electrons. Therefore, the polarizability of ions with f valence electrons (lanthanides) would be different from that of Y^{3+} ion.

From Figures 2 and 3, it is evident both empirically and experimentally that there is a strong correlation between the dopant polarizability and the kinetics of the ordering process. It was argued by Fung et al that due to the dependance of the kinetics of aging on dopant ionic radii, the conductivity decay occurs by some sort of cation ordering mechanism [20]. However, our results clearly show that the dopant cations affect the kinetics of the ordering process due to their effect on the nature of the vacancy arrangement in the oxygen sublattice. The aging process itself is governed by the vacancy ordering and the displacement of oxygen ions in the lattice.

III. Anion Ordering and its Effect on Conductivity Activation Energy

From the discussion in the previous section, it is clear that the polarizability of the cation sublattice affects the nature of distribution of oxygen ions in the anion sublattice. It has been determined by Jacobs et al that the stability of the intermediate interstitials was lowered by increasing the cation polarizability [16]. This is consistent with our results shown in Table 1. The fraction of oxygen ions in the 32f interstitial positions is lowest for the structure doped with the Dy ion which is the most polarizable among the studied dopants (Section II). This clearly has a significant effect on the conductivity mechanism, as discussed in the subsequent sections.

The activation energy values measured for aged and unaged samples with different dopants are shown in Table 2. The activation energies for different compositions of Er are given in Table 3. The activation energies for the aged samples of 25 DySB, 30 ErSB, 35 ErSB, and 40ErSB were not calculated because of slow kinetics of aging for these compositions. From Tables 2 and 3, it is clear that the activation energy is less for the aged samples. This is a surprising result because the conductivity of the aged samples is orders of magnitude less than that of unaged samples. This can however be explained by the concept of the minimum energy path discussed previously. In the aged samples, the oxygen ions occupy the interstitial sites, which are the intermediate states in the minimum energy path of tetrahedral-octahedral-tetrahedral transport. Therefore, the conductivity activation energy of the ordered structure is less because most of the oxygen ions are in the intermediate stages of the path.

However, in the ordered structure, transport of oxygen ions is more constrained because of the ordered <111> vacancy arrangement (Figure 1, Ordered Structure). Therefore, the probability of oxygen ions in the 32f positions to have a neighboring vacant 8c site in the transport from one tetrahedral site to an adjacent tetrahedral site (in <100> direction) is much lower than that in a disordered structure where all the 8c sites have an equal probability to be vacant or occupied (Figure 1, Disordered Structure). Consequently, the number of actual jumps of oxygen ions into vacancies is limited, leading to lower ionic conductivity.

In the disordered structure, the oxygen ions are randomly distributed between the regular and the interstitial sites. The conductivity activation energy is greater due to less oxygen ions in the interstitial sites. However, the transport of oxygen ions into the vacant sites is statistically

greater. Due to the disordered nature of the lattice the number of possible jump directions is higher as shown in Figure 1 (Disordered Structure). This leads to a significantly higher conductivity.

The migration of the oxygen ions in the lattice involves breaking of ionic bonds between the cations and the anions. Therefore, the conductivity activation energy depends upon the strength of the ionic bond. The activation energy should therefore be higher for the structure with stronger ionic bond. The force constant, K, for an ionic bond is given by

$$K = \frac{2z_1 z_2 e^2}{\pi \varepsilon_o r_o^3} \qquad (1)$$

where z_1e and z_2e are the effective charges of anion and cation respectively (2e and 3e in our case), and r_o is the interatomic distance, or the bond distance. From the above equation, it is clear that the force constant depends upon the equilibrium distance between the cations and the anions. This distance will vary with the nature of the distribution of oxygen ions in the anion sublattice.

In the fluorite structure, if the oxygen ion occupies the regular 8c site, the bond distance would be $\sqrt{3}/4a$, and if the oxygen ion occupies the interstitial 32f position, the bond distance would be 0.606a (Fig. 4). From the fractional distribution of oxygen ions in 8c and 32f sites (Table 1), the equilibrium bond distances in the ordered and disordered structure have been determined. The calculated bond lengths and the force constants of the bonds in ordered and disordered structures are shown in Table 4. For all the cases, the force constants for the disordered structures is higher than those of the corresponding ordered structure, consistent with their observed higher activation energies.

The thermal vibrational frequency of the atoms also depends on the bond strength. The frequency of vibration of atoms is given by

$$\nu = \frac{1}{2\pi}\sqrt{\frac{K}{M_r}} \qquad (2)$$

where K is the force constant of the ionic bond, and M_r is the effective mass of the oscillating system, given by $M_r = m_1 m_2/(m_1 + m_2)$, where m_1 and m_2 are the respective atomic weights of anion and cation. From the calculated values of force constants, the vibrational frequencies of oxygen ions have been calculated and are shown in Table 4.

From the Table, it is clear that the vibrational frequency in the disordered structures is higher than that in the corresponding ordered structures by about 15 percent. This is as expected and is consistent with the higher slope obtained for the disordered structures both in the Differential Thermal Analysis (DTA) [4] and the mean square atomic displacement of oxygen ions versus temperature [14].

III. Effect of Structure on Conductivity Pre-Exponential Factor

Nowick et al [23] computed the pre-exponential term in conductivity for various families of ionic conductors. According to them, the pre-exponential term will vary with three possible structural arrangements.

- The structure is completely disordered and the defects are equally likely to occupy any site at any instant of time. This is the case with the unaged structure.
- Most of the carriers are bound at specific defect sites, while only a small fraction of carriers are free to move. This is the case of aged structure, in which the majority of oxygen ions are not mobile because of lack of vacancies at nearest neighbor positions. In this case, the value

of the pre-exponential will be less than that for the disordered case. The pre-exponential also depends on the square of the jump distance, which is lower for aged sample. Due to the ordered structural arrangement of the mobile anion sublattice, and the occupancy of oxygen ions in the intermediate stages of conduction paths, the conductivity acivation energy would be lower than that of the disordered structure, what we experimentally observed.

- Almost all the carriers are bound to various traps and only those that are released contribute to conductivity. Fung et al use this theory to explain aging phenomenon. They argue that dopant cations become ordered and act as traps for oxygen ions [20]. In this case, the pre-exponential will be greater in the ordered structure than that in the disordered case, and the activation energy will be higher, contrary to the observed results (Tables 2 and 3).

Therefore, it is not possible to explain the lower conductivity and lower conductivity activation energy of the ordered structure without considering vacancy ordering and the occupancy of oxygen ions in interstitial sites.

The temperature dependence of conductivity is given by [23]

$$\sigma T = A \exp(-E_A/kT) \qquad (3)$$

where σ is the oxygen ion conductivity, T is the temperature, E_A is the activation energy, and k is the Boltzmann Constant. The pre-exponential term A is given by

$$A = n\lambda^2 (ze)^2 \nu c_i / 6Vk \qquad (4)$$

where n is the number of directions in which the jump may occur, λ is the jump distance, ze is the electronic charge of the conducting species, ν is the pre-exponential of the jump frequency, c_i is the concentration of the charge carriers, and V is the volume of the unit cell. The variables appearing in the above equation depend primarily on the structure of the anion sublattice. From

the neutron diffraction data (Table 1) and the structural models for the ordered structure, we can determine these variables for ordered and disordered structures, and compare the pre-exponentials for the two structures.

Jump Frequency

The pre-exponential of the jump frequency, ν is given by $\nu = \nu_o \exp(\Delta S_m/k)$, where ν_o is the characteristic vibrational frequency (shown in Table 4) and ΔS_m is the entropy of activation. The values of $\Delta S_m/k$ have been calculated to be in the range of 2 to 3 for simple defect systems [23]. Since this factor causes no significant change in the order of the pre-exponential values, it has been ignored in our calculations. The values of ν_o are typically in of the order of 10^{13} consistent with our calculated values [23].

Jump Distance

Figure 4 illustrates the positions and the atomic coordinates of the sites important in the conduction mechanism. The figure is not drawn to scale with respect to the ionic sizes of the ions and is used primarily for calculating the jump distances in the unit cell. From the Figure, we can see that a single ionic jump constitutes the movement of an oxygen ion from position A to position E. We have discussed previously that the most favorable path for this event is A--B--C--D--E. However, from Table 1, we can see that there is a significant fraction of oxygen ions in 32f sites (positions B and D) in the disordered structures, and the majority of oxygen ions occupy those positions in the ordered structures.

From Figure 4, we can see that the length of the body diagonal <111> is $a\sqrt{3}$, where a is the lattice parameter. Therefore, the length of AC is $a\sqrt{3}/4$ (= 0.433a). Therefore, the jump distance from the 8c site at A to the 8c site at E is $a\sqrt{3}/2$ which is 0.866a. The distance between B (0.313, 0.313, 0.313) to C (0.5, 0.5, 0.5) is $(a\sqrt{3}/8)\bullet(0.375/0.313)$ which is 0.260a. Therefore, the jump distance from the 32f site at B to the 8c site at E is 0.260a + 0.433a, which equals 0.693a.

Figure 5 illustrates the mechanism of a <100> jump from an occupied 8c site to an adjacent empty 8c site. Each of these tetrahedral positions is surrounded by a cation tetrahedron with four 32f positions, one at each face of the tetrahedron. For our calculations we will consider a jump to have occurred only if an anion moves from a tetrahedron, either from the central 8c or associated 32 f positions, to an adjacent vacant tetrahedron. Referring to Figure 4, this means that a jump will have occurred if an anion moves from either position A or B to position E, but not if an anion moves from position D to position E since the latter is only displacement of the anion within the same tetrahedron.

From the calculations shown above, it is clear that if the oxygen ion is in an 8c site, the effective jump distance is 0.866a. If it is in the 32f site displaced from the same 8c site, the jump distance to the nearest neighbor empty tetrahedral site is 0.693a. From Table 1, we can see that there is an occupancy of oxygen ions in both 8c and 32f sites. Therefore, we have to take into account, the fraction of oxygen ions in these two sites, and the respective jump distances to calculate the effective jump distance.

Jump Directions

From our previous work [19] we determined the most likely model for an ordered structure with oxygen ions displaced from the 8c to 32f positions. A section of the model (four unit cells) is shown in Figure 6 (without displacements) and involves a <111> vacancy superlattice similar to the Sillen model shown in Figure 1. However, from Figure 6, it can be observed that this model also includes a <110> ordering of vacancies. As discussed in previous sections, this <110> ordering is preferred by bismuth ions. Therefore, this type of an ordered structure (with both <111> and <110> vacancy ordering) is most likely to form.

From Figure 6, each oxygen ion has two nearest neighbor vacancies along the <100> directions. Thus, it appears that the number of possible jump directions in this ordered structure is two. However, if we consider the positional ordering in the structure, *i.e.*, the displacement of each of the oxygen ions from an 8c site to an adjacent 32f site, the number of jump directions would be limited to one. This is illustrated in Figure 7, which shows a two dimensional section of the superlattice. Let us consider the jump directions of an oxygen ion O1 which has only occupancy ordering. It has two nearest neighbor vacancies, V1 and V2 in <100> directions. Therefore, an oxygen ion at O1 is likely to have two possible jump directions - O1--C1--V1 and O1--C2--V2 as shown in Figure 7(a). In Figure 7 (b), the displacement of oxygen ions into 32f sites (positional ordering) is also shown . In this case, the oxygen ion at O1 is displaced to the interstitial site f1. Consequently, the only possible jump direction is f1--C1--V1. The other direction would not constitute a single jump, because the oxygen at f1 would have to first come back to O1. Neutron diffraction studies have shown that the occupancy of oxygen ions in 8c sites is negligible. Therefore, it is very unlikely to have two jump directions in the ordered structure. Due to occupancy (<111> and <110> vacancy ordering) and positional ordering (<111> displacements of oxygen ions), the number of possible jump directions is limited to one. In the

disordered case, the number of possible jump directions is six with two equivalent paths for each jump resulting in twelve equivalent paths.

Charge and Concentration of Charge Carriers

In the disordered structure, all the oxygen ions are equally likely to perform a jump because there is an equal probability for each of the eight 8c sites to be vacant at any instant. Therefore, the mole fraction of charge carriers in the disordered case is 1, because all the oxygen ions are mobile charge carriers. However, since each site is occupied by only 3/4 oxygen ion the effective charge carried is only 1.5e.

For the ordered structure, (Figures 1 and 6) we can see that two oxygen ions (out of six) per unit cell can carry out a successful jump to a nearest neighbor tetrahedral site in the <100> directions. Therefore, the mole fraction of charge carriers in this case is 0.333. Since there is no fractional occupancy of sites, the effective charge carried is 2e.

Pre-Exponential

The variables appearing in the equation for the pre-exponential for both ordered and disordered structures are summarized in Table 5 except for ν, whose values are shown in Table 4. From the tables, it is clear that there is a significant difference in the parameters that affect the pre-exponential between the ordered and disordered structures. The 8c and 32f terms shown in Table 5 are the fraction of oxygen ions in those two sites respectively. These fractions were taken from the occupancies of oxygen ions shown in Table 1.

The jump distance, λ shown in Table 5 will vary with the lattice parameter (a) and the distribution of the oxygen ions between the 8c and 32f positions. The lattice parameters and the corresponding actual jump distances for each of the dopants are shown in Table 6.

From Table 6, it can be noted that the difference between the jump distances of ordered and disordered structures is highest for Yb and Er doped structures, and lowest for the Dy doped structures. This clearly is consistent with the difference in kinetics of aging for structures with different dopants. In addition, we know that the ordered structure does not form completely for the case of Dy. That is while the occupancy of 8c vs. 32f sites (from neutron diffraction data) is accounted for in our calculations, the fact that the larger radii and more polarizable dopants result in ordering at a much slower rate means that the <111> ordering of vacancies may not have fully occurred after 300 hours at 500°C. However, the calculations were carried out for this case assuming the same model for the sake of comparison.

The calculated pre-exponentials based on the above approach are shown in Table 7. From the Table, it is clear that the conductivity pre-exponential values of ordered structures are an order of magnitude less than those of the disordered structures.

The conductivity pre-exponentials (A) were measured from the Arrhenius plots of ordered and disordered structures in the temperature range 200-400 °C and are shown in Table 8. From this table, it can be observed that the measured pre-exponentials for the ordered structures are lower than those for the disordered structures and they are of the same order of magnitude as those calculated from the interstitial transport model (Table 7).

There is clearly some difference between the calculated and observed values. This could be due to the approximate nature of the model in which several assumptions had to be made to simplify the calculations. For example, the fraction of oxygen ions occupying the 48i sites was neglected for the calculation of jump distances and the entropy of activation was neglected in the calculation of pre-exponentials.

Further investigations are necessary to refine this model. However, it can be observed from Tables 7 and 8 that the ratios of the calculated pre-exponentials of ordered to disordered structures is in close agreement to the corresponding ratios of the measured pre-exponentials indicating the validity of this approach.

Mechanistically, the preferential occupancy of oxygen ions in the 32f sites leading to a lower conductivity activation energy is consistent with the theoretical calculations of Koto et al for ionic transport in the fluorite structure [15]. Mathematically, the lower value of the pre-exponential term, A of the ordered structure results in a lower value of activation energy (Equation 3) even though the conductivity is much lower. Therefore, the interstitial transport mechanism explains the anomalous decrease in activation energies for the ordered structures.

CONCLUSIONS

The ionic transport mechanism in the Fluorite structure involves a path that is more complicated than a simple hopping mechanism between the regular tetrahedral sites along <100> directions. This is due to the presence of vacant octahedral positions which lead to more favorable paths involving the displacement of oxygen ions towards the central vacant position along the <111> directions. This has been confirmed experimentally in δ-Bi_2O_3 by neutron diffraction studies, which show extensive displacements of oxygen ions along the <111> directions. Due to the disordered defect fluorite structure of cubic bismuth oxide, this mechanism

leads to an exceptionally high ionic conductivity. Due to the high polarizability of the bismuth ion, the pure bismuth oxide has an extensive long-range disorder in the anion sublattice. By doping with less polarizable lanthanide elements, the extent of short range <111> vacancy ordering increases. Consequently, the ionic conductivity of doped cubic bismuth oxides decreases with increasing dopant concentration.

The time dependent decay in conductivity below the order-disorder transition temperature, observed in doped bismuth oxides, occurs due to the long range ordering of oxygen vacancies along <111> directions and the displacement of almost all the oxygen ions from the regular 8c positions to the interstitial 32f positions, also along <111> directions. The kinetics of aging depend upon the ionic radius and polarizability of the dopant cation. The low temperature conductivity activation energies of the ordered bismuth oxides are lower than those of the corresponding disordered cases. This is due to the structural changes in the mobile anion sublattice. The calculated and measured pre-exponentials for the disordered structures are higher than those of the corresponding ordered structures for all the studied compositions. Therefore, the observed reduction in activation energies can be explained by oxygen vacancy ordering and the displacement of oxygen ions to the intermediate states in the conduction path. The activation energy results and the neutron diffraction results are consistent with the general model for interstitial transport mechanism in Fluorite structures. This study confirms the fact that the distribution of oxygen ions, both in terms of occupancy (ordering of vacancies) and displacement (interstitial positions), affects the conductivity of cubic bismuth oxides.

ACKNOWLEDGEMENT

We would like to thank the US Department of Energy (Contract # DE-AC26-99FT40712) for supporting this work.

REFERENCES

[1]T. Takahashi, H. Iwahara and Y. Nagai, *J. Appl. Electrochem*., **2** 97-104 (1972)

[2]T. Takahashi, H. Iwahara, T. Arao, *J. Appl. Electrochem*., **5** 187-195 (1975)

[3]M. J. Verkerk, A. J. Burggraaf, *Solid State Ionics*, **3/4** 463-467 (1981)

[4]E. D. Wachsman, N. Jiang, D. M. Mason, and D. A. Stevenson, *Proc. Electrochem. Soc*., **15** 89-11 (1989)

[5]N Jiang, R. M. Buchanan, F. E. G. Henn, A. F. Marshall, D. A. Stevenson, and E. D. Wachsman, *Mater. Res. Bull*., **29**, 247-254 (1994).

[6]N. Jiang, R. M. Buchanan, D. A. Stevenson, W. D. Nix, Li Ji-Zhou, and Yang Ji-Lian, *Materials Letters* **22**, 215-219 (1995)

[7]N. Jiang and E. D. Wachsman, *J. Am. Ceram. Soc*. **82**, 3057-3064 (1999)

[8]E. D. Wachsman, S. Boyapati, M. J. Kaufman, and N. Jiang, *Solid State Ionic Devices : Proc. Electrochem.* Soc. 42-51 (1999)

[9]V. G. Gattow and H. Schroder, *Z. Anorg. Allg. Chem*., **318** 197 (1962)

[10]P. D. Battle, C. R. A. Catlow, J. W. Heap, and L. M. Moroney, *J. Solid State Chem*., **63** 8 (1986)

[11]P. D. Battle, C. R. A. Catlow, J. W. Heap, and L. M. Moroney, *J. Solid State Chem*., **67** 42 (1987)

[12]L. G. Sillen, Ark. Kemi. Mineral. Geol. **12A** 18 (1937)

[13]B. T. M. Willis, Acta Crystallogr. **18** 75 (1965)

[14]S. Boyapati, E. D. Wachsman, and B. C. Chakoumakos, submitted to *Solid State Ionics*

[15]K. Koto, H. Schultz, and R. A. Huggins, *Solid State Ionics*, **5** 355-365 (1980)

[16]P. W. M. Jacobs and D. A. Mac Donaill, *Solid State Ionics*, **23** 279-293 (1987)

[17]P. W. M. Jacobs and D. A. Mac Donaill, *Solid State Ionics*, **23** 295-305 (1987)

[18]P. W. M. Jacobs and D. A. Mac Donaill, *Solid State Ionics*, **23** 307-318 (1987)

[19]E. D. Wachsman, S.Boyapati, M. J. Kaufman, and N. Jiang, Accepted for publication, *J. Amer. Cer. Soc.*

[20]K. Z. Fung, J. Chen, and A. V. Virkar, *J. Am. Ceram. Soc* **76**, 2403-2418, (1993)

[21]N.Jiang, Thesis, Stanford University

[22] K. Shirao, T. Iiada, K. Kazuko, and Y. Iwadate, *J. Alloys and Compounds* **281** 163-168 (1998)

[23]A. S. Novick, W-K. Lee, and H. Jain, *Solid State Ionic*s **28-30**, 89-94 (1988)

FIGURE CAPTIONS

Figure 1. Interstitial transport mechanism

Figure 2. Time constant for aging as a function of dopant polarizability

Figure 3. Time constant for aging as a function of dielectric constant at different temperatures

Figure 4. Fluorite Structure

Figure 5. Jump from one tetrahedron to an adjacent empty tetrahedron in <100> direction

Figure 6. Vacancy superlattice

Figure 7. Illustration of Jump directions in an ordered structure with occupancy and positional ordering

Table 1. Comparison of Structural Parameters of Aged and Unaged Structures *

Dopant	Time Constant for Aging (h)	0ccupancy in 8c sites		Occupancy in 32f sites		Change in occupancy due to aging
		Unaged	Aged	Unaged	Aged	1- 8c(aged)/8c(unaged)
Yb	4.177	1.08	0.06	1.62	2.64	0.9444
Er	24.823	1.16	0.08	1.54	2.62	0.9310
Y	53.789	1.17	0.10	1.53	2.60	0.9145
Ho	79.412	1.26	0.37	1.44	2.33	0.7063
Dy	170.00	1.32	1.14	1.38	1.56	0.1363

*The remaining fraction (0.3) of oxygens in the anion sublattice occupy the 48 i sites

Table 2. Low Temperature Activation Energy of $(Bi_2O_3)_{0.75}(M_2O_3)_{0.25}$

M_2O_3	Unaged (ev)	Aged at $500^{O}C$ (ev)
Yb_2O_3	1.23	1.10
Er_2O_3	1.22	1.09
Y_2O_3	1.22	1.07
Tm_2O_3	1.22	1.08
Ho_2O_3	1.26	1.13
Dy_2O_3	1.19	

Table 3. Low Temperature Activation Energy of $(Bi_2O_3)_{1-x}(Er_2O_3)_x$

x(%)	Unaged (ev)	Aged at 500^{O}C (ev)
15	1.24	1.02
20	1.25	1.04
25	1.22	1.09
30	1.22	
35	1.20	
40	1.21	

Table 4. Calculated Bond Strength and Vibrational Frequencies for Ordered and Disordered Structures

Dopant	Structure	Bond Length, Å	Force Constant, N/m	Vibrational Frequency, $s^{-1}x10^{12}$
Yb	Disordered	2.644	597.83	9.81
	Ordered	2.966	423.49	8.26
Er	Disordered	2.624	611.60	10.02
	Ordered	2.965	423.92	8.34
Y	Disordered	2.625	610.90	12.22
	Ordered	2.963	424.78	10.20
Ho	Disordered	2.597	630.88	10.21
	Ordered	2.879	463.06	8.75
Dy	Disordered	2.581	642.68	10.35
	Ordered	2.639	601.23	10.01

Table 5. Comparison of variables affecting A

	Disordered Structure	Ordered Structure
λ	$[0.866 \bullet 8c_{(unaged)} + 0.693 \bullet 32f_{(unaged)}]a/3$	$[0.866 \bullet 8c_{(aged)} + 0.693 \bullet 32f_{(aged)}]a/3$
n	6	1
Ze	1.5e	2e
C_i	1	0.333

Table 6. Calculated Jump Distances in Ordered and Disordered Structures

Dopant	Lattice Parameter, a Å	Jump Distance in the Disordered Structure, Å	Jump Distance in the Ordered Structure, Å
Yb	5.474	3.755	3.433
Er	5.484	3.787	3.445
Y	5.492	3.795	3.457
Ho	5.493	3.825	3.543
Dy	5.501	3.849	3.792

Table 7. Calculated Pre-Exponentials for Unaged and Aged $(Bi_2O_3)_{0.75}(M_2O_3)_{0.25}$

Dopant	$A_{(\text{Disordered Structure})}$ $x10^5$ $(ohm.cm)^{-1}K$	$A_{(\text{Ordered Structure})}$ $x10^5$ $(ohm.cm)^{-1}K$	$\frac{A_{(\text{Ordered Structure})}}{A_{(\text{Disordered Structure})}}$
Yb	34.33	2.40	0.069
Er	36.36	2.46	0.067
Y	44.35	3.02	0.068
Ho	37.61	2.72	0.072
Dy	38.44	3.54	0.092

Table 8. Measured Pre-exponentials for Unaged and Aged $(Bi_2O_3)_{0.75}(M_2O_3)_{0.25}$

Dopant	$A_{(\text{Disordered Structure})}$ $x10^5$ $(ohm.cm)^{-1}K$	$A_{(\text{Ordered Structure})}$ $x10^5$ $(ohm.cm)^{-1}K$	$\frac{A_{(\text{Ordered Structure})}}{A_{(\text{Disordered Structure})}}$
Yb	93.88	6.73	0.071
Er	52.39	1.98	0.037
Y	114.78	9.54	0.083
Ho	42.45	3.59	0.084
Dy	62.67	4.89	0.078

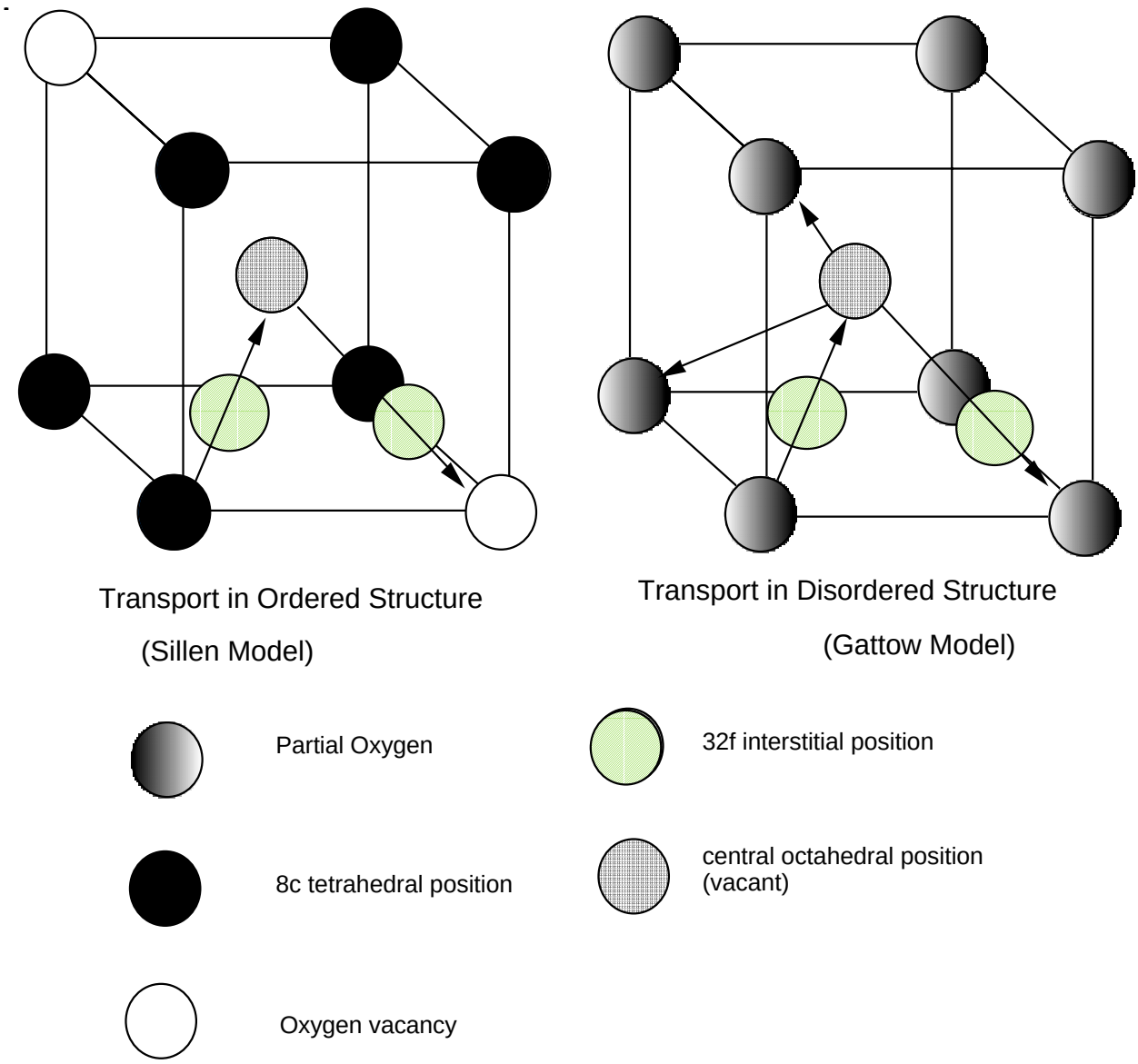

Figure 1. Transport mechanism in ordered and disordered structures

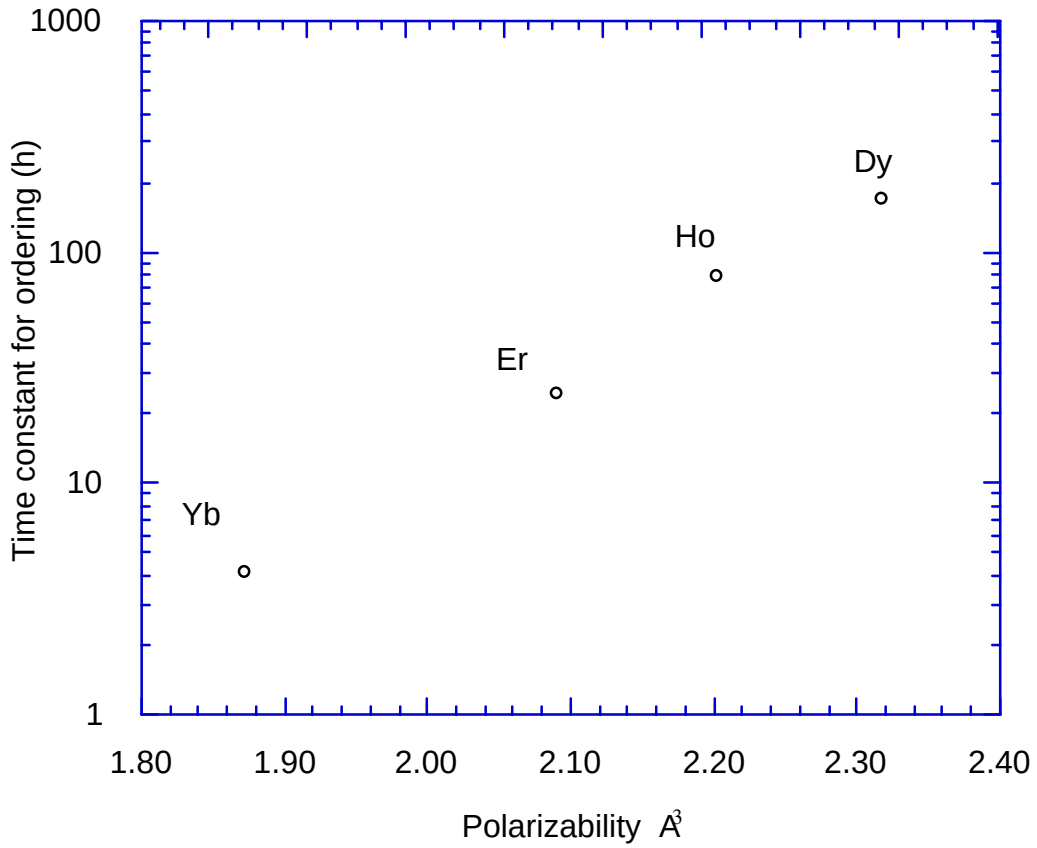

Figure 2. Time constant for aging as a function of dopant polarizability

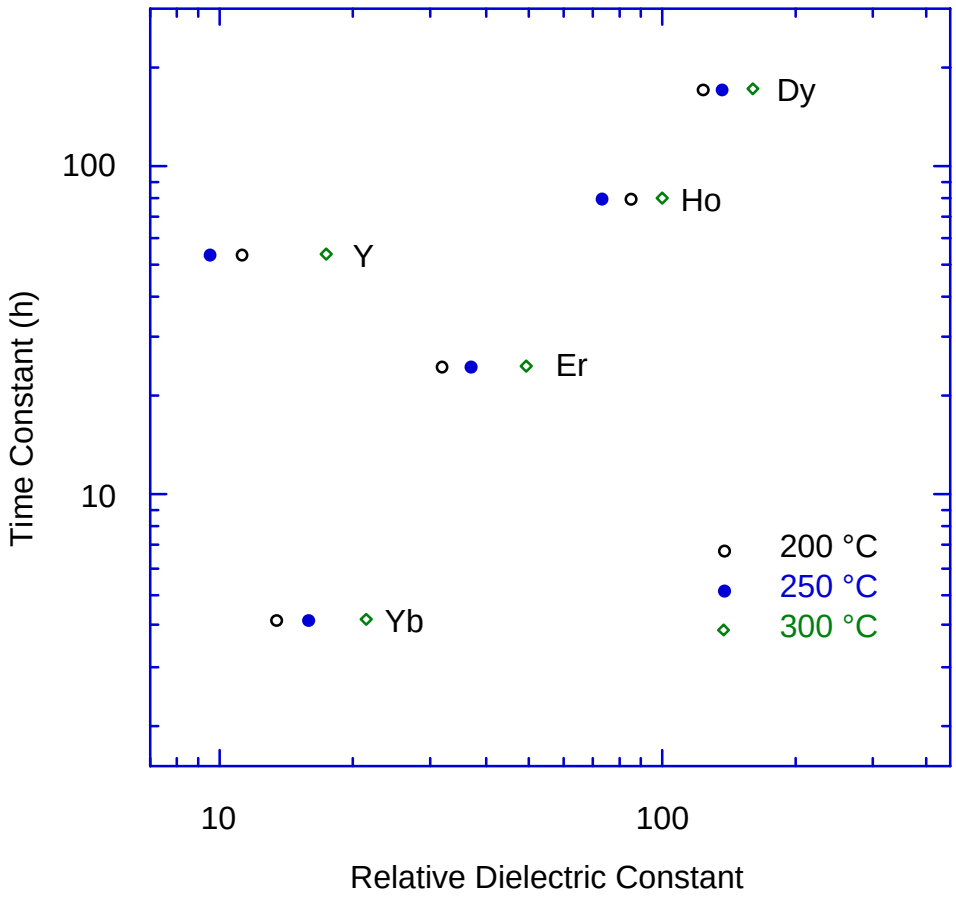

Figure 3. Time constant for aging as a function of dielectric constant at different temperatures

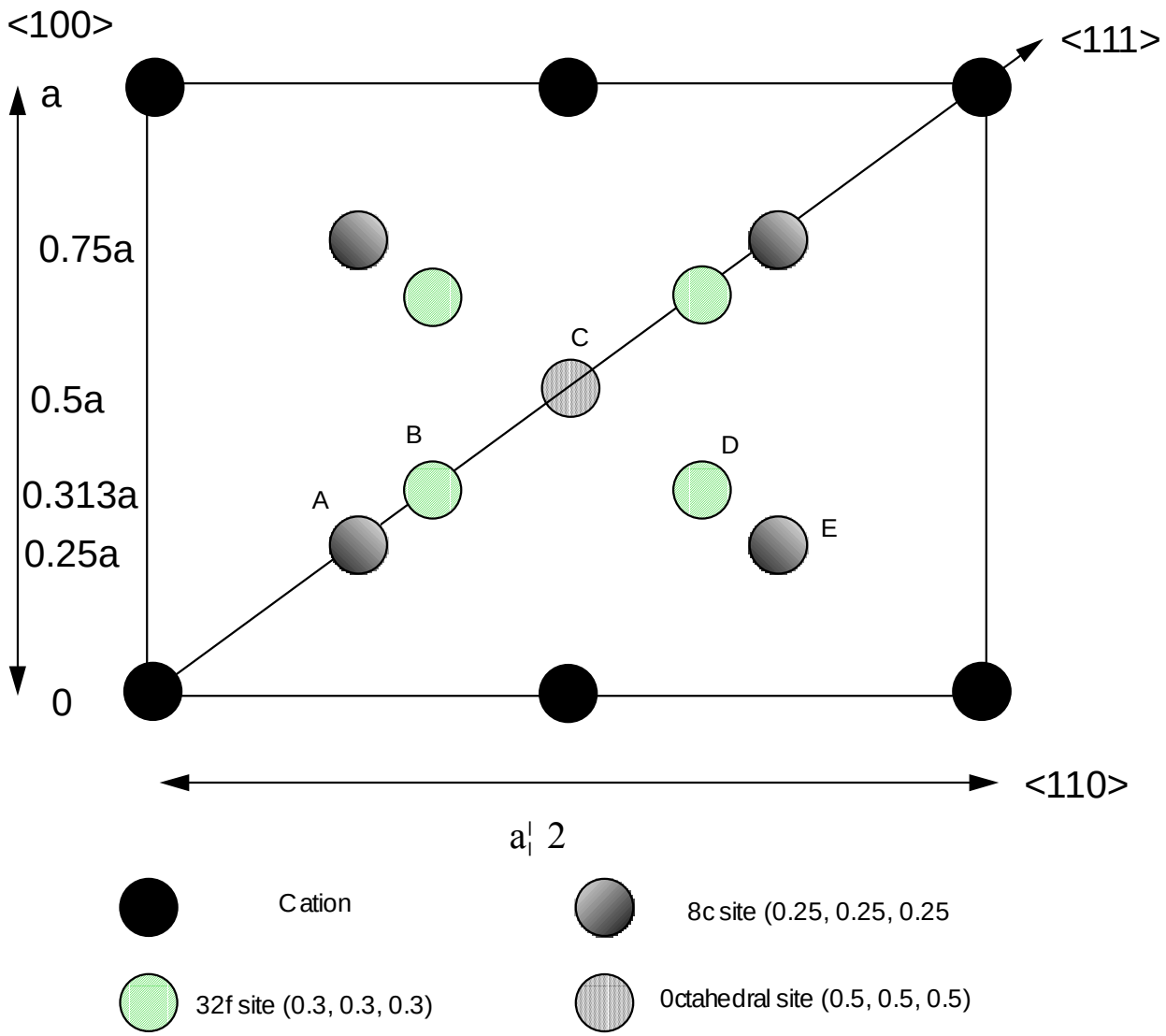

Figure 4. Fluorite structure indicating the jump distances

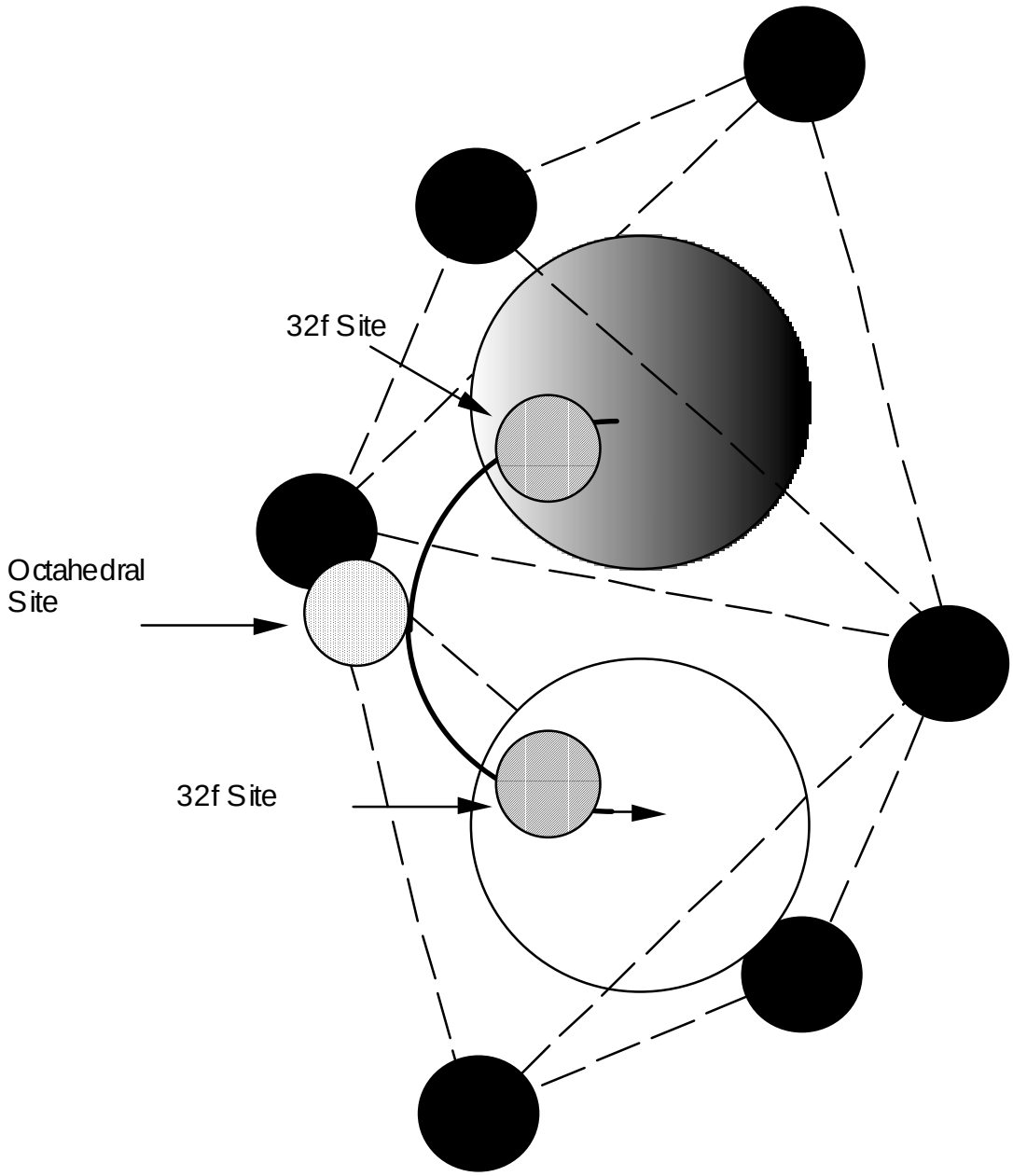

Figure 5. Transport mechanism between adjacent tetrahedral sites

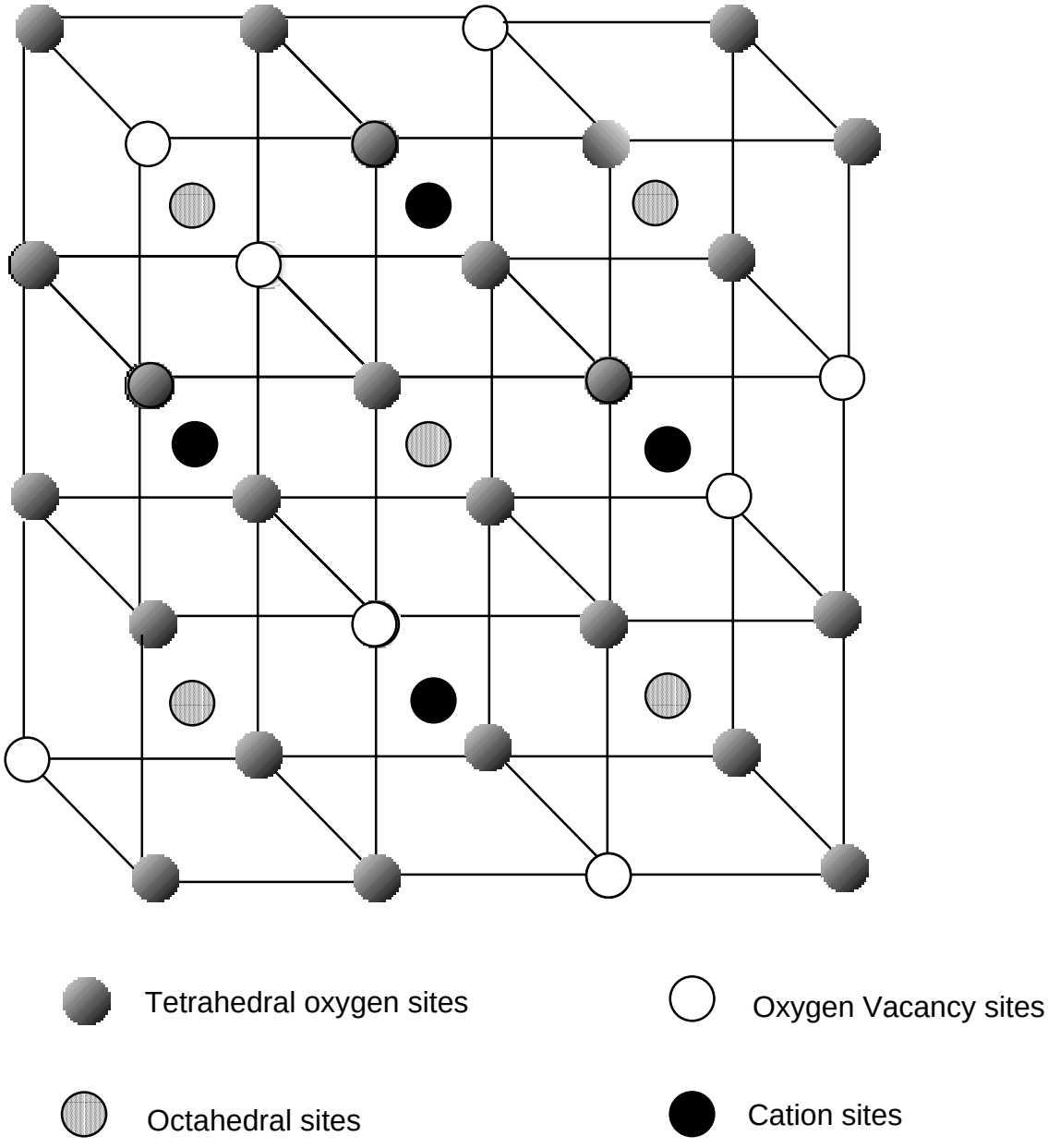

Figure 6. Vacancy superlattice with both <111> and <110> vacancy arrangement

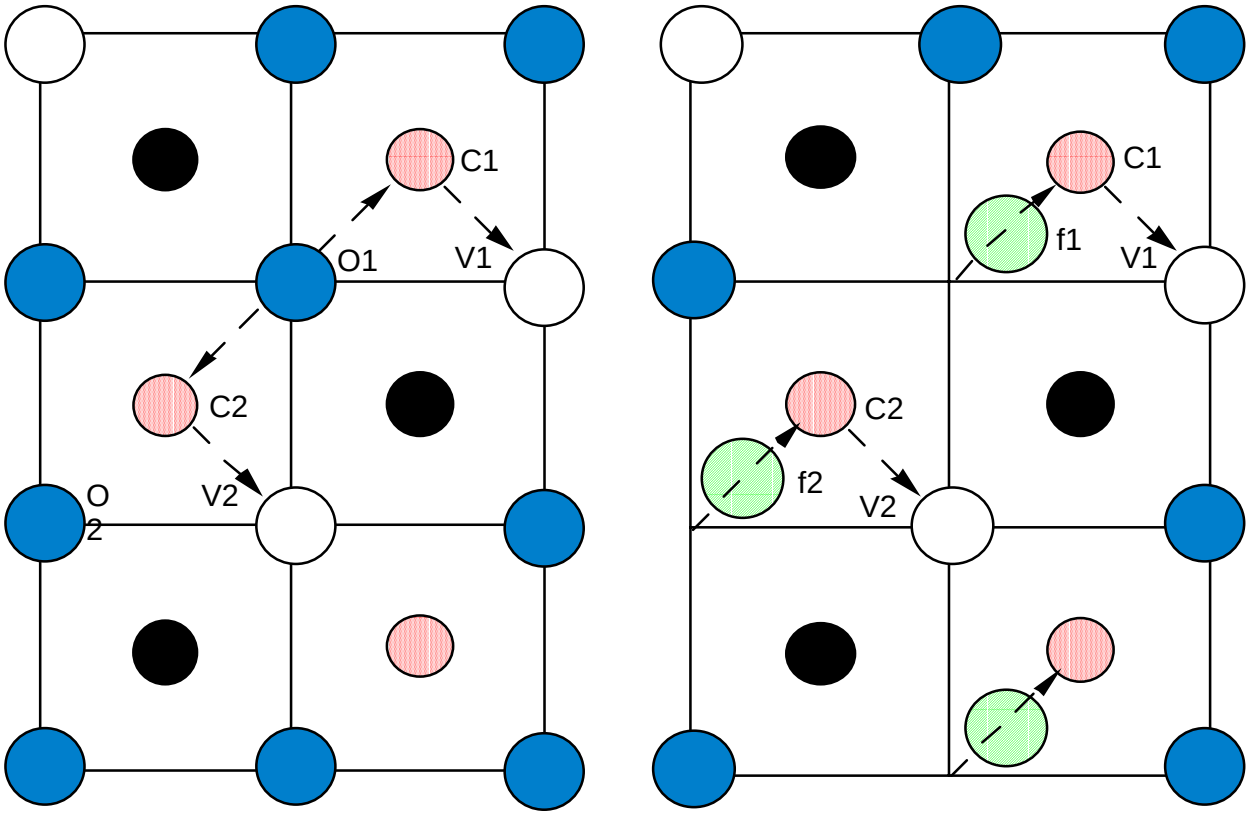

a. Occupancy ordering

b. Occupancy and positional ordering

Figure 7. Jump directions in ordered structures with (a) occupancy ordering and (b) occupancy and positional ordering